Mon. Not. R. Astron. Soc. **334,** 355–368 (2002)

The pattern speed of the OH/IR stars in the Milky Way

Victor P. Debattista,[1★] Ortwin Gerhard[1] and Maartje N. Sevenster[2]
[1]*Astronomisches Institut, Universität Basel, Venusstrasse 7, CH-4102 Binningen, Switzerland*
[2]*RSAA/MAAAO, RSAA/MSSSO, Cotter Road, Weston ACT 2611, Australia*

Accepted 2002 March 13. Received 2002 March 12; in original form 2001 July 16

ABSTRACT

We show how the continuity equation can be used to determine pattern speeds in the Milky Way Galaxy (MWG). This method, first discussed by Tremaine & Weinberg in the context of external galaxies, requires projected positions, (l,b), and line-of-sight velocities for a spatially complete sample of relaxed tracers. If the local standard of rest (LSR) has a zero velocity in the radial direction ($u_{\rm LSR}$), then the quantity that is measured is $\Delta V \equiv \Omega_{\rm p} R_0 - V_{\rm LSR}$, where $\Omega_{\rm p}$ is the pattern speed of the non-axisymmetric feature, R_0 is the distance of the Sun from the Galactic centre and $V_{\rm LSR}$ is the tangential motion of the LSR, including the circular velocity. We use simple models to assess the reliability of the method for measuring a single, constant pattern speed of either a bar or spiral in the inner MWG. We then apply the method to the OH/IR stars in the ATCA/VLA OH 1612-MHz survey of Sevenster et al., finding $\Delta V = 252 \pm 41\,{\rm km\,s^{-1}}$, if $u_{\rm LSR} = 0$. Assuming further that $R_0 = 8\,{\rm kpc}$ and $V_{\rm LSR} = 220\,{\rm km\,s^{-1}}$, this gives $\Omega_{\rm p} = 59 \pm 5\,{\rm km\,s^{-1}\,kpc^{-1}}$ with a possible systematic error of perhaps $10\,{\rm km\,s^{-1}\,kpc^{-1}}$. The non-axisymmetric feature for which we measure this pattern speed must be in the disc of the MWG.

Key words: Galaxy: bulge – Galaxy: disc – Galaxy: kinematics and dynamics – Galaxy: structure – galaxies: spiral.

1 INTRODUCTION

Our position within the Milky Way Galaxy (MWG) has made study of its large-scale structure and dynamics difficult. This is partly due to the position of the Sun within the dust layer of the MWG, as well as to the difficulty of determining distances. Nevertheless, in recent years, considerable progress has been made in understanding our Galaxy.

It is now clear that the MWG is a barred galaxy, as was first proposed by de Vaucouleurs (1964). Evidence of this comes from the *COBE*/DIRBE near-infrared light distribution (Weiland et al. 1994; Dwek et al. 1995; Binney, Gerhard & Spergel 1997), star count asymmetries (Nakada et al. 1991; Whitelock & Catchpole 1992; Sevenster 1996; Nikolaev & Weinberg 1997; Stanek et al. 1997; Hammersley et al. 2000), gas dynamics (Peters 1975; Cohen & Few 1976; Liszt & Burton 1980; Gerhard & Vietri 1986; Mulder & Liem 1986; Binney et al. 1991) and the large microlensing optical depth towards the bulge (Paczynski et al. 1994; Zhao, Rich & Spergel 1996). A recent review of the structure of the bulge and disc can be found in Gerhard (2001).

The principle dynamical parameter of a bar is its pattern speed, $\Omega_{\rm p}$, as it determines the orbital structure of stars in the disc. Bar pattern speeds can be parametrized by the distance-independent ratio $\mathcal{R} \equiv D_{\rm L}/a_{\rm B}$, where $D_{\rm L}$ is the Lagrangian radius at which the gravitational and centrifugal forces cancel out in the bar rest-frame ($D_{\rm L}$ is usually approximated by the axisymmetric corotation radius) and $a_{\rm B}$ is the bar semimajor axis. A bar is termed fast when $1.0 \leqslant \mathcal{R} \leqslant 1.4$. Knowledge of bar pattern speeds constrains the dark matter (DM) content of disc galaxies: Debattista & Sellwood (1998, 2000) argue that fast bars require that the disc they inhabit must be maximal, in the sense that the luminous disc provides most of the rotational support in the inner galaxy. Some evidence for fast bars comes from hydrodynamical models of gas flow, particularly at the shocks. Three such studies are: NGC 1365 ($\mathcal{R} = 1.3$, Lindblad, Lindbland & Athanassoula 1996), NGC 1300 ($\mathcal{R} = 1.3$, Lindblad & Kristen 1996), and NGC 4123 ($\mathcal{R} = 1.2$, Weiner, Sellwood & Williams 2001).

In the MWG, $\Omega_{\rm p}$ can be estimated by comparing hydrodynamical models of the inner MWG with the observed longitude–velocity, (l, v), diagram. Several such studies have been carried out: Englmaier & Gerhard (1999) found $D_{\rm L} = 3.5 \pm 0.5\,{\rm kpc}$, $\Omega_{\rm p} = 59 \pm 2\,{\rm km\,s^{-1}\,kpc^{-1}}$ and $\mathcal{R} = 1.2 \pm 0.2$, while Fux (1999) found $D_{\rm L} = 4$–$4.5\,{\rm kpc}$ and $\Omega_{\rm p} = 35$–$45\,{\rm km\,s^{-1}\,kpc^{-1}}$ and the preferred model of Weiner & Sellwood (1999) had $D_{\rm L} = 5.0\,{\rm kpc}$, $\Omega_{\rm p} = 41.9\,{\rm km\,s^{-1}\,kpc^{-1}}$ and $\mathcal{R} = 1.4$. Binney et al. (1991) interpreted the (l, v) diagram for H I, CO and CS emission using orbits in a barred potential with $\Omega_{\rm p} = 63\,{\rm km\,s^{-1}\,kpc^{-1}}$. Another method for measuring $\Omega_{\rm p}$ in the MWG involves the identification of the action

★E-mail: debattis@astro.unibas.ch

© 2002 RAS

of resonances: Binney, Gerhard & Spergel (1997) suggested that a local density maximum along the minor axis seen in the dust-corrected infrared *COBE*/DIRBE data could be identified with the location of a Lagrange point, which gave $\Omega_p = 65 \pm 5\,\mathrm{km\,s^{-1}\,kpc^{-1}}$, having assumed $\mathcal{R} \simeq 1.2$ and given the value of a_B from the deprojection. Dehnen (1999) argued that the bimodal distribution of stellar velocities in the solar neighbourhood, as observed by *HIPPARCOS*, is due to the action of the outer Lindblad resonance (OLR), whereby he obtained $\Omega_p = 53 \pm 3\,\mathrm{km\,s^{-1}\,kpc^{-1}}$. Sevenster (1999) suggested that features in the distribution of OH/IR stars can be used to locate the corotation and inner Lindblad resonances, giving $\Omega_p \sim 60\,\mathrm{km\,s^{-1}\,kpc^{-1}}$ ($\mathcal{R} \gtrsim 1.4$). The differences in these pattern speed measurements reflect uncertainties in viewing geometry, a_B, rotation curve and bar axis ratio.

The MWG also has spiral structure in it, which is less well constrained. Even the number of arms, whether two or four, continues to be an issue of some discussion. Vallée (1995) reviews a variety of different observational tracers, and concludes that the spirals are four-armed, logarithmic and have a pitch angle, $p \simeq 12° \pm 1°$. More recently, Drimmel & Spergel (2001) found that a two-arm spiral structure dominates the non-axisymmetric near-infrared emission.

The pattern speeds of spirals are generally quite poorly constrained. When a bar is present, as in the MWG, the expectation that spirals are driven by it (e.g. Sanders & Huntley 1976) would seem to require that the bar and spirals share a common pattern speed. This idea appears to be further reinforced by the observation that many such spirals connect with the bar ends. Sellwood & Sparke (1988), however, presented *N*-body simulations in which bars and spirals had different pattern speeds, but with the spirals still generally connected to the bar ends. Tagger et al. (1987) and Sygnet et al. (1988) proposed that the pattern speeds of the bar and spirals are non-linearly resonantly coupled, with the corotation of the bar marking the inner Lindblad resonance of the spiral. Toomre's (1981) swing amplification theory of spiral structure formation requires a radially (and possibly temporally) varying pattern speed. Modal theories of spiral formation, on the other hand, depend on a (nearly) constant spiral pattern speed in space (but not necessarily in time, see Bertin & Lin 1996). Measurements of spiral pattern speeds in external galaxies are still quite few, generally assume a radially constant Ω_p and tend to give conflicting results. For example, the spiral pattern speed in M81 has been measured in a variety of ways but so far no unique pattern speed has been found (see discussion in Canzian 1993).

The situation is not much better in the MWG. Morgan (1990) was able to model the distribution of pulsars within roughly 10 kpc of the Sun with spirals of $\Omega_p = 13.5\,\mathrm{km\,s^{-1}\,kpc^{-1}}$, regardless of the arm multiplicity. On the other hand, Amaral & Lépine (1997), using the positions and ages of young open clusters within ~ 5 kpc of the Sun, estimated $\Omega_p \simeq 20\,\mathrm{km\,s^{-1}\,kpc^{-1}}$. Mishurov & Zenina (1999) used the velocity field of a sample of Cepheids which were less than 5 kpc from the Sun to conclude that the Sun is displaced outwards from the corotation by ~ 0.1 kpc (then $\Omega_p \simeq \Omega_\odot \simeq 27\,\mathrm{km\,s^{-1}\,kpc^{-1}}$).

A direct method for measuring Ω_p in systems satisfying the continuity equation was developed by Tremaine & Weinberg (1984). This method has successfully been applied to four barred galaxies so far: NGC 936 ($\mathcal{R} = 1.4 \pm 0.3$, Merrifield & Kuijken 1995), NGC 4596 ($\mathcal{R} = 1.15^{+0.38}_{-0.23}$, Gerssen, Kuijken & Merrifield 1998), NGC 7079 ($\mathcal{R} = 0.9 \pm 0.15$, Debattista & Williams 2001) and NGC 1023 ($\mathcal{R} = 0.77^{+0.43}_{-0.22}$, Debattista, Corsini & Aguerri 2002). In view of the spread in previous measurements of pattern speeds in the MWG, it is worth considering whether this method may not also be applied to it. Kuijken & Tremaine (1991) have already derived an equivalent of the Tremaine–Weinberg method for the MWG; their main goal was to constrain the radial motion of the local standard of rest (LSR). Applying this method to the H I distribution, they found that pattern speeds from $\Omega_p = 0$ to $\Omega_\odot$ are possible for an LSR with a radial velocity of from $u_{LSR} = -4$ to $8\,\mathrm{km\,s^{-1}}$.

In this paper, we explore the Tremaine–Weinberg method for the MWG. This method, unlike others, has the considerable advantage of being model-independent. In the general case, the only assumption made is that the non-axisymmetric density distribution is in stationary cylindrical rotation [i.e. $\Omega_p = \Omega_p(\rho)$, where ρ is the distance from the Galactic centre]. While this assumption breaks down in some cases (e.g. if the MWG disc is strongly interacting with a companion), it is expected to be a very good approximation inside the solar circle. Because we also wish to apply the method to real data, we have made a number of simplifying assumptions. For example, we assume that there is one unique pattern speed in the inner MWG; if this is not the case, then some density and asymmetry weighted average pattern speed is measured. The value of Ω_p obtained depends sensitively on the assumed radial velocity of the LSR; however this dependence can be stated explicitly. The method requires complete samples of tracers: one such sample is obtained from the ATCA/VLA OH 1612-MHz survey of OH/IR stars.

In Section 2, we derive the three-dimensional version of the Tremaine–Weinberg method for the MWG, with the solar and LSR motion taken into account. We test the method in Section 3, using simple models, exploring under what circumstances the method works best. In Section 4, we introduce the ATCA/VLA OH 1612-MHz survey, and describe how we selected a sample of older, relaxed OH/IR stars from it. We also discuss our completeness corrections for the survey data. Then in Section 5, we present the pattern speed analysis for our sample of OH/IR stars. Because the integrals in the Tremaine–Weinberg method measure asymmetries between positive and negative longitude, they are susceptible to noise and/or observational bias; therefore in Section 5, we present corroborating evidence for the signal we find. Finally, in Section 6, we discuss our results in terms of MWG structure and prospects for using the same method with future data sets.

2 THE TREMAINE–WEINBERG METHOD FOR THE MILKY WAY

Starting from the continuity equation and the assumption that the visible surface density, μ, of a barred (or otherwise non-axisymmetric) disc depends on time, t, in the following simple way:

$$\mu(x, y, t) = \mu(\rho, \psi - \Omega_p t), \tag{1}$$

where (x, y) are arbitrary Cartesian coordinates in the plane of the disc, and (ρ, ψ) are the corresponding polar coordinates, Tremaine & Weinberg (1984) showed that the pattern speed, Ω_p, can be written as:

$$\Omega_p \sin i = \frac{\int_{-\infty}^{\infty} h(Y) \int_{-\infty}^{\infty} V_{los}(X, Y)\mu(X, Y)\,\mathrm{d}X\,\mathrm{d}Y}{\int_{-\infty}^{\infty} h(Y) \int_{-\infty}^{\infty} X\mu(X, Y)\,\mathrm{d}X\,\mathrm{d}Y}. \tag{2}$$

Here, V_{los} is the line-of-sight (minus the systemic) velocity, $h(Y)$ is

an arbitrary continuous weight function, i is the inclination angle and (X, Y) are galaxy-centered coordinates along the apparent major and minor axes of the disc, respectively. The Tremaine–Weinberg (TW) method needs a tracer of the non-axisymmetric feature which satisfies the continuity equation. The old stellar population in undisturbed SB0-type disc galaxies provides an ideal tracer of the surface density. The short lifetimes of massive stars, however, precludes their use as tracers. Moreover, gas cannot be used as a tracer because of its conversion between atomic and molecular states, although modelling may be used to describe such conversions (Bienaymé et al. 1985).

2.1 Two dimensions

We now seek to derive an equivalent to the TW method for the MWG. Our position within the MWG disc gives a unique viewing geometry which does not permit the standard TW method of equation (2) to be used. As shown by Kuijken & Tremaine (1991), however, it is still possible to use the continuity equation to derive an expression for a pattern speed in the MWG. Here, we re-derive their two-dimensional expression before considering the three-dimensional case. Assuming equation (1) holds, the continuity equation in the plane of the disc can be written:

$$\Omega_{\rm p}\left(y\frac{\partial\mu}{\partial x}-x\frac{\partial\mu}{\partial y}\right)+\nabla\cdot(\mu\boldsymbol{v})=0. \tag{3}$$

Switching to Sun-centered cylindrical coordinates (R, l), (where l is the usual Galactic longitude and R is the distance from the Sun), this becomes:

$$\Omega_{\rm p}\left[-R_0\sin l\frac{\partial\mu}{\partial R}+\left(1-\frac{R_0\cos l}{R}\right)\frac{\partial\mu}{\partial l}\right] +\frac{1}{R}\frac{\partial(R\mu v_R)}{\partial R}+\frac{1}{R}\frac{\partial(\mu v_l)}{\partial l}=0. \tag{4}$$

In this equation, (v_R, v_l) is the velocity in the (R, l) frame and R_0 is the distance of the Sun from the Galactic centre. Typically, the component v_l is not available; fortunately, this term drops out after an integration over l:

$$\Omega_{\rm p}\left(-R_0\frac{\partial}{\partial R}\int_0^{2\pi}\mu\sin l{\rm d}l-\frac{R_0}{R}\int_0^{2\pi}\mu\sin l{\rm d}l\right) +\frac{1}{R}\frac{\partial}{\partial R}\int_0^{2\pi}\mu v_R R\,{\rm d}l=0. \tag{5}$$

If we now multiply by $Rg(R)$, where $g(R)$ is an arbitrary function vanishing at the Sun, and integrate over R, we obtain, after some rearrangement:

$$\Omega_{\rm p}R_0=\frac{\int_0^\infty\int_0^{2\pi}\mu f(R)v_R\,{\rm d}l\,{\rm d}R}{\int_0^\infty\int_0^{2\pi}\mu f(R)\sin l\,{\rm d}l\,{\rm d}R}, \tag{6}$$

where we have assumed that $\mu g(R)$ goes to zero at infinity and $f(R)\equiv R\partial g/\partial R$. All the quantities on the right-hand side of the above equation are observable.

In the case of discrete tracers, the surface density gets replaced by a sum over delta functions and the above expression is replaced by:

$$\Omega_{\rm p}R_0=\frac{\sum_i f(R_i)v_{R,i}}{\sum_i f(R_i)\sin l_i}. \tag{7}$$

Thus $f(R)$ can be thought of as a detection probability for the discrete tracers.

In equation (6) above, we integrated l from 0 to 2π. However, if the non-axisymmetric part of μ is limited to the range $[-l_0, l_0]$, it is then trivial to show that these integration limits are sufficient, because axisymmetric components do not contribute to the integrals, and all surface terms resulting from the l integrals vanish by symmetry. It is necessary, however, that the integrals extend from $-l_0$ to l_0 (i.e. integration in the range $[-l_1, l_2]$ with $l_1\neq l_2$ gives incorrect results).

When the bar is either along or perpendicular to the line of sight, the numerator and denominator of equation (7) are zero, and $\Omega_{\rm p}R_0$ cannot be determined. This is to be compared with the standard TW equation, where $\Omega_{\rm p}$ cannot be measured for a bar along the apparent major or minor axis of the disc.

2.2 Three dimensions

In 3D, the derivation is more or less the same. The Sun-centered spherical polar coordinates are now (r, l, b), with (l, b) being the standard galactic coordinates and r the distance from the Sun. Following a triple integral much in the spirit of the 2D case, we obtain:

$$\Omega_{\rm p}R_0=\frac{\int_0^\infty\int_{-b_0}^{+b_0}\int_{-l_0}^{+l_0}f(r)\mu\cos b v_r\,{\rm d}l\,{\rm d}b\,{\rm d}r}{\int_0^\infty\int_{-b_0}^{+b_0}\int_{-l_0}^{+l_0}f(r)\mu\cos^2 b\sin l\,{\rm d}l\,{\rm d}b\,{\rm d}r}, \tag{8}$$

where b_0 must be such that all the non-axisymmetric parts are included. If the system is symmetric about the mid-plane, then the b integral can extend over the region $[0, \pm b_0]$ only: data of this kind are easier to obtain. A discrete version of this equation is given by:

$$\Omega_{\rm p}R_0=\frac{\sum_i f(r_i)v_{r,i}}{\sum_i f(r_i)\sin l_i\cos b_i}\equiv\frac{\mathcal{K}(l_0)}{\mathcal{P}(l_0)}. \tag{9}$$

where we have introduced a new notation for the integrals. (Note that one factor of $\cos b$ drops out because of the Jacobian in the delta functions.) In the limit that all the tracers are in a plane, equation (9) reduces to equation (7) of the 2D case.

Both $\mathcal{P}$ and $\mathcal{K}$ are defined as integrals/sums over l ranging from $-l_0$ to l_0. Because $\sin l$ and v_r change sign across $l=0$, the integrals will partially cancel out. Thus $\mathcal{P}$ and $\mathcal{K}$ largely measure a difference across $l=0$. When the difference is small, $\mathcal{P}$ and $\mathcal{K}$ are small and the measured $\Omega_{\rm p}R_0$ will be poorly determined. This can be seen from the expression for the variance in $\Omega_{\rm p}R_0$: $(\sigma_{[\Omega_{\rm p}R_0]}/\Omega_{\rm p}R_0)^2=(\sigma_{\mathcal{K}}/\mathcal{K})^2+(\sigma_{\mathcal{P}}/\mathcal{P})^2$. To be more explicit by what we mean by small, we define $\mathcal{P}_\pm\equiv\int_0^\infty\int_{-b_0}^{+b_0}\int_0^{\pm l_0}f(r)\mu\cos^2 b\sin l\,{\rm d}l\,{\rm d}b\,{\rm d}r$, with a similar definition for $\mathcal{K}_\pm$. (In this notation $\mathcal{P}=\mathcal{P}_+-\mathcal{P}_-$ and similarly for $\mathcal{K}$.) Then we introduce the variables

$$A_{\mathcal{K}}=\frac{|\mathcal{K}|}{|\mathcal{K}_-|+|\mathcal{K}_+|},\qquad A_{\mathcal{P}}=\frac{|\mathcal{P}|}{|\mathcal{P}_-|+|\mathcal{P}_+|}. \tag{10}$$

These two parameters, which take values in the range [0,1], quantify the degree of global asymmetry in the system. When $A_{\mathcal{P}}=A_{\mathcal{K}}=0$, no asymmetry signal is present (but note that the system need not be axisymmetric, or even symmetric in projection)

while when $A_{\mathcal{P}} = A_{\mathcal{K}} = 1$ the observed system is maximally asymmetric. In Section 3, we use simple models to explore the dependence of measurement errors on $A_{\mathcal{P}}$ and $A_{\mathcal{K}}$.

2.3 More complicated density distributions

Several complications may arise, including multiple pattern speeds, non-stationary pattern speeds, solar motion, etc. Here we discuss issues related to violations of the density assumption in equation (1), deferring discussion of solar motion to Section 2.4. Possible violations of equation (1) include the following.

(i) Multiple pattern speeds. The MWG has a bar and spirals, perhaps also a small lopsidedness; almost certainly all have different pattern speeds. To understand how these will affect the measurement, we suppose that there are n non-axisymmetric features superposed, so that equation (1) becomes $\mu(x,y,t) = \sum_{i=0}^{n} \mu_i(\rho, \psi - \Omega_i t)$. Each of these asymmetries gives rise to integrals $\mathcal{P}_i$ and $\mathcal{K}_i$. Then, by the linearity of the continuity equation, we can write $R_0 \sum_i \Omega_i \mathcal{P}_i = \sum_i \mathcal{K}_i \equiv \mathcal{K}$. Dividing both sides by $\mathcal{P} \equiv \sum_i \mathcal{P}_i$, we obtain $R_0 \bar{\Omega} = \mathcal{K}/\mathcal{P}$, where $\bar{\Omega}$ is the average of the different pattern speeds, weighted by the $\mathcal{P}_i$ values. Thus the average is weighted by both the asymmetry and the density (because if $\mu_1 = s\mu_2$ then $\mathcal{P}_1 = s\mathcal{P}_2$). Therefore, small perturbations to the disc density do not contribute very significantly to $\bar{\Omega}$. However, because the $\mathcal{P}_i$ values can be either positive or negative, $\bar{\Omega}$ is not limited to values in the range min (Ω_i) and max (Ω_i) (unless all the $\mathcal{P}_i$ values have the same sign). If distances are available, $f(R)$ can be varied, to test for such cancellations; otherwise, strong changes in the slope of $\mathcal{P}$ as a function of l_0 may be used to test for cancellations.

Note that winding spiral arms are a special case of the multiple pattern speed situation. In this case, $\Omega_{\rm p}$ is a continuously varying function of distance from the Galactic centre. This case is discussed further in Section 6.1.

(ii) Radial oscillations. If such oscillations were present, equation (1) would become $\mu(x,y,t) = \mu[\rho + \rho_1 \mathrm{e}^{-i\omega(t-t_0)}, \psi - \Omega_{\rm p} t]$, where we assume ρ_1 is small. The time-derivative term in the continuity equation therefore becomes

$$\frac{\partial \mu}{\partial t} \simeq -\Omega_{\rm p} \frac{\partial \mu}{\partial \psi} - i\omega\rho_1 \, \mathrm{e}^{i\omega t_0} \frac{\partial \mu}{\partial R} \equiv A_0 + A_1. \tag{11}$$

The ratio $|A_1/A_0|$ is then given by $\omega\rho_1/(2\Omega_{\rm p} R_{\rm d})$, where, for concreteness, we have assumed that the disc is exponential with scalelength $R_{\rm d}$ and the azimuthal density variation is of the form $\mu(R)\,\mathrm{e}^{2i\psi}$. For a simple estimate, we assume $\omega \sim \max(\kappa) \sim 2\Omega$. Therefore we obtain $|A_1/A_0| \sim V_c \rho_1/\Omega_{\rm p} R_{\rm d} \rho$; at $\rho = 1$ kpc, if the circular velocity is $220\,\mathrm{km\,s^{-1}}$, $\Omega_{\rm p} = 60\,\mathrm{km\,s^{-1}\,kpc^{-1}}$ and $R_{\rm d} = 2.1$ kpc (Bissantz & Gerhard 2002), we obtain $|A_1/A_0| \sim 1.7\rho_1\,\mathrm{kpc}^{-1}$. Thus radial oscillations with amplitude larger than about 100 pc will strongly interfere with the measurement of pattern speeds using the TW method. However, radial oscillations are expected to be strongly Landau damped, and it would be very surprising if the MWG exhibits large radial oscillations.

(iii) Growing amplitudes. In this case, we can replace equation (1) with $\mu(x,y,t) = \mu_0(\rho) + \mu_1(\rho, \psi - \Omega_{\rm p} t)\,\mathrm{e}^{\alpha t}$, where $\alpha > 0$ ($\alpha < 0$) represents a growing (damped) feature. The term $\mu_0(\rho)$ is included to make explicit the fact that the density of the feature grows at the expense of a background axisymmetric disc (for which $\mathcal{P} = \mathcal{K} = 0$), to conserve the total mass. The time-derivative term is now replaced by

$$\frac{\partial \mu}{\partial t} = -\Omega_{\rm p} \mathrm{e}^{\alpha t} \frac{\partial \mu}{\partial \psi} + \alpha \mu_1 \, \mathrm{e}^{\alpha t} \equiv A_0 + A_1. \tag{12}$$

It is possible to propagate the term in $\alpha\mu_1$ through the calculation, giving, in the 2D case

$$\Omega_{\rm p} R_0 \mathcal{P} + \alpha \int_0^{\infty} \int_0^{2\pi} R g(R) \mu_1 \, \mathrm{d}l \, \mathrm{d}R = \mathcal{K}. \tag{13}$$

Equation (13) contains both $f(R)$ and $g(R)$, and therefore requires distance data for a solution. Lacking distances, we estimate the interference from growing features by the ratio $|A_1/A_0|$, which, for an $m = 2$ azimuthal density variation, is given by $|\alpha|/(2\Omega_{\rm p})$. Thus the growth term is important when the growth rate is of the order of the pattern speed (in which case it is safe to ignore damping). As rapid growth is mostly restricted to the low-amplitude, linear regime, while $A_{\mathcal{P}}$ can only be large enough for an accurate measurement once growth is nearly saturated, we expect that rapid growth is unlikely to significantly interfere with pattern speed measurements.

The most important growing structures are spirals. If they are modal, they can grow even when tightly wound. The theoretically computed growth rates vary substantially; e.g. the fastest growing two-arm modes in the flat-rotation, cut-out discs of Evans & Read (1998) have $0.03 \lesssim \alpha/2\Omega_{\rm p} \lesssim 0.29$.

(iv) Time-varying pattern speeds. In this case, equation (1) gets replaced by $\mu(x,y,t) = \mu[\rho, \psi - \Omega_{\rm p}(t) t]$. Although this introduces a new term, proportional to $t(\partial\Omega_{\rm p}/\partial t)$, it also changes the angle derivative to one in the bar rest frame. A simple transformation to a time t' in which the moment of observation is $t' = 0$ recovers equation (8). Thus a time-varying pattern speed does not disturb the TW method.

We have considered several violations of the density condition of equation (1). Of these, perhaps the most likely are growing spirals, but it is unclear how rapidly the spirals are growing. Most likely, if spirals are of sufficient amplitude to give large signals, then their growth rate cannot be too large. This may be sorted with more detailed data on the MWG density distribution than we currently have, such as will be available with future astrometric missions. For the present work, we have assumed that there are no (strong) non-axisymmetric structures with rapidly growing amplitudes.

2.4 Solar motion

We derived equation (8) for an inertial frame. Any radial velocities that can be measured will be heliocentric, and therefore the motion of the Sun needs to be taken into account. The Sun's velocity can be decomposed into two parts: a motion of the local standard of rest, $\boldsymbol{v}_{\rm LSR}$, and the peculiar motion of the Sun relative to the LSR, $\boldsymbol{v}_{\odot,\rm pec}$. We assume that the motion of the LSR consists of two parts; $\boldsymbol{v}_{\rm LSR} = u_{\rm LSR}\hat{\boldsymbol{x}} + V_{\rm LSR}\hat{\boldsymbol{y}}$, where $\hat{\boldsymbol{x}}$ is in the direction towards the Galactic centre and $\hat{\boldsymbol{y}}$ is the in-plane tangential direction. Then, if velocities in the heliocentric frame are labelled as $\boldsymbol{v}_i'$, we can write $v_{r,i} = (\boldsymbol{v}_i' + \boldsymbol{v}_\odot)\cdot\hat{\boldsymbol{r}}_i = v_{r,i}' + \boldsymbol{v}_{\odot,\rm pec}\cdot\hat{\boldsymbol{r}}_i + \boldsymbol{v}_{\rm LSR}\cdot\hat{\boldsymbol{r}}_i = v_{r,i}' + \boldsymbol{v}_{\odot,\rm pec}\cdot\hat{\boldsymbol{r}}_i + V_{\rm LSR}\sin l_i \cos b_i + u_{\rm LSR}\cos l_i \cos b_i$. Thus equation (9) can be rewritten:

$$\Delta V \equiv \Omega_{\rm p} R_0 - V_{\rm LSR} = \frac{\sum_i f(r_i)(v_{r,i}' + \boldsymbol{v}_{\odot,\rm pec}\cdot\hat{\boldsymbol{r}}_i)}{\sum_i f(r_i)\sin l_i \cos b_i} - u_{\rm LSR}\frac{\sum_i f(r_i)\cos l_i \cos b_i}{\sum_i f(r_i)\sin l_i \cos b_i} \equiv \frac{\mathcal{K}}{\mathcal{P}} - u_{\rm LSR}\frac{\mathcal{S}}{\mathcal{P}}. \tag{14}$$

This equation, which is the 3D form of the TW equation derived by Kuijken & Tremaine (1991), is used in the analysis of the OH/IR star sample below. It contains two quantities, $V_{\rm LSR}$ and $u_{\rm LSR}$ which must be determined from other data. Here, $V_{\rm LSR}$ includes the circular velocity; Reid et al. (1999) measured $V_{\rm LSR} = 219 \pm 20\,{\rm km\,s^{-1}}$ for $R_0 = 8\,{\rm kpc}$, from the apparent proper motion of Sgr A*, while from a similar measurement Backer & Sramek (1999) measured $V_{\rm LSR} = 234 \pm 7\,{\rm km\,s^{-1}}$. The uncertainty in $u_{\rm LSR}$ leads to a much larger uncertainty in ΔV, largely because $\mathcal{S}$ depends on the values of $\cos l_i$, which do not cancel across $l = 0$. The TW equation for external galaxies is similarly sensitive to the relative motion of the observer and the observed galaxy, but in that case reflection symmetry is used to minimize this sensitivity. In the absence of distance information, no similar symmetry argument can be deployed in the MWG. The solar peculiar motion, $\boldsymbol{v}_{\odot,{\rm pec}}$, has been measured with *HIPPARCOS* data by Dehnen & Binney (1998). They found $\boldsymbol{v}_{\odot,{\rm pec}} = (U_0, V_0, W_0) = (10.00, 5.25, 7.17) \pm (0.36, 0.62, 0.38)\,{\rm km\,s^{-1}}$. (These correspond to velocity components that are radially inwards, in the direction of Galactic rotation and vertically upwards, respectively.) In the absence of a radial motion of the LSR, we will then be measuring $\Delta V \equiv \Omega_{\rm p} R_0 - V_{\rm LSR}$, i.e. the negative of the solar velocity in the rest frame of the bar.

In the coordinate system we are working in, a star moving away from the LSR has a positive v_r; inside the solar circle, such stars will primarily be at positive l. Therefore, if a positive ΔV is measured, this will correspond to a non-axisymmetric feature in the inner MWG with a pattern speed $\Omega_{\rm p} > \Omega_\odot$, which must therefore be rotating in the same sense as the disc.

The variance in ΔV due to the errors in the measured peculiar velocity of the Sun is given by:

$$\sigma^2_{\Delta V} = \sigma^2_{U_0} \frac{\left[\sum_i f(r_i) \cos l_i \cos b_i\right]^2}{\mathcal{P}^2} + \sigma^2_{V_0} + \sigma^2_{W_0} \frac{\left[\sum_i f(r_i) \sin b_i\right]^2}{\mathcal{P}^2} \tag{15}$$

(where we have assumed that errors in position measurements are insignificant). Note that, in this expression, the dominant term is the coefficient of $\sigma^2_{U_0}$, because $\cos l$ is everywhere positive in the range $-\pi/2 \leqslant l \leqslant \pi/2$.

3 TESTS

We now test the TW method on some simple models. Our goal is not so much to test for specific structures expected in the MWG, as such an approach would say more about our models, which we would like to keep simple. Rather, our goal here is to learn how reliable the TW method is under various *observational* constraints, such as the number of discrete tracers, signal strength, restricted ranges of l, etc. Errors from sources specific to our application are discussed in Section 5.

Models used to test the TW method need to have velocity fields which preserve the assumed density distribution, i.e. the assumption of equation (1) needs to remain valid. However, because the continuity equation is purely kinematic, a model density distribution need not generate the potential required by the kinematics. Here we test the method on models for a bar and a spiral, with application to the OH/IR stars in the ATCA/VLA OH 1612-MHz survey of Sevenster et al. (1997a,b, 2001) in mind. Because OH/IR stars are concentrated in the inner MWG, our tests assume that the non-axisymmetric structure is inside the Solar circle. We assume throughout that measurements of l, b and v_r for individual stars have only small errors, which we ignore, as is appropriate for this survey.

3.1 Bar pattern speeds

Tests of the method for a realistic bar can be obtained from N-body simulations. We tested equation (9) for a selection of the bars in the fully self-consistent, N-body simulations of Debattista & Sellwood (2000), who measured $\Omega_{\rm p}$ from the time rate of change of the phase of the $m = 2$ Fourier component of the disc density. Here we present the results of several experiments using their 'maximum disc' simulation at $t = 650$, which is shown in Fig. 1, when the bar was fast ($\mathcal{R} = 1.1 \pm 0.2$). At this time, $a_{\rm B} = (2.6 \pm 0.6) R_{\rm d}$ (where $R_{\rm d}$ is the disc scalelength), which is about twice the size of the MWG bar. The viewer therefore was placed at $4 \leqslant R_0/R_{\rm d} \leqslant 5$ (within the disc). The angle of the bar to the Sun-centre line, ψ, was varied in the expected range ($20° \leqslant \psi \leqslant 30°$). The angle l_0, within which the integrals $\mathcal{P}$ and $\mathcal{K}$ were evaluated, was varied in the range $30° \leqslant l_0 \leqslant 60°$. The simulation included 102 000 disc particles; here we describe two experiments in which samples of 500 particles were selected. In the first experiment, particles were drawn using $f(r)$ a Gaussian with $\bar{r} = 2.25 R_{\rm d}$ and $\sigma_r = 0.7 R_{\rm d}$. The second experiment used a cosine probability: $f(r) = \cos[(r/R_{\rm max}) \times (\pi/2)]$ with $R_{\rm max} = 6 R_{\rm d}$ for $r \leqslant R_{\rm max}$ and $f(r) = 0$ otherwise.

Fig. 2 plots the results, from which it is clear that the best results are obtained at large $A_{\mathcal{P}}$ and $A_{\mathcal{K}}$; because the Gaussian probability selects particles in a more limited radial range, it often gives larger $A_{\mathcal{P}}$ and $A_{\mathcal{K}}$ and smaller errors. However, the cosine probability is likely to be more realistic for a flux-density-limited sample of tracers, as it preferentially selects nearby objects over distant ones. Fig. 2 show that, when $A_{\mathcal{P}} \gtrsim 0.15$ and $A_{\mathcal{K}} \gtrsim 0.15$, the expected error is on average ~ 17 per cent, and never worse than 40 per cent.

Variations in ψ, l_0 and R_0 mattered to the errors in ΔV only insofar as they changed $A_{\mathcal{P}}$ and $A_{\mathcal{K}}$. For the Gaussian $f(r)$ experiment, increasing R_0 decreased $A_{\mathcal{P}}$ and $A_{\mathcal{K}}$, with a corresponding increase in the fractional error. However, changes

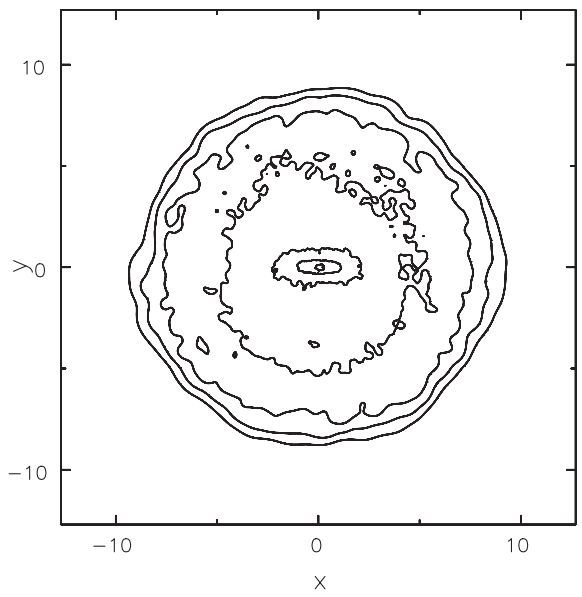

Figure 1. Contours of projected disc density of the N-body barred system used in the tests. Contours are logarithmicaly spaced. This is the 'maximum disc' simulation of Debattista & Sellwood (2000) at $t = 650$.

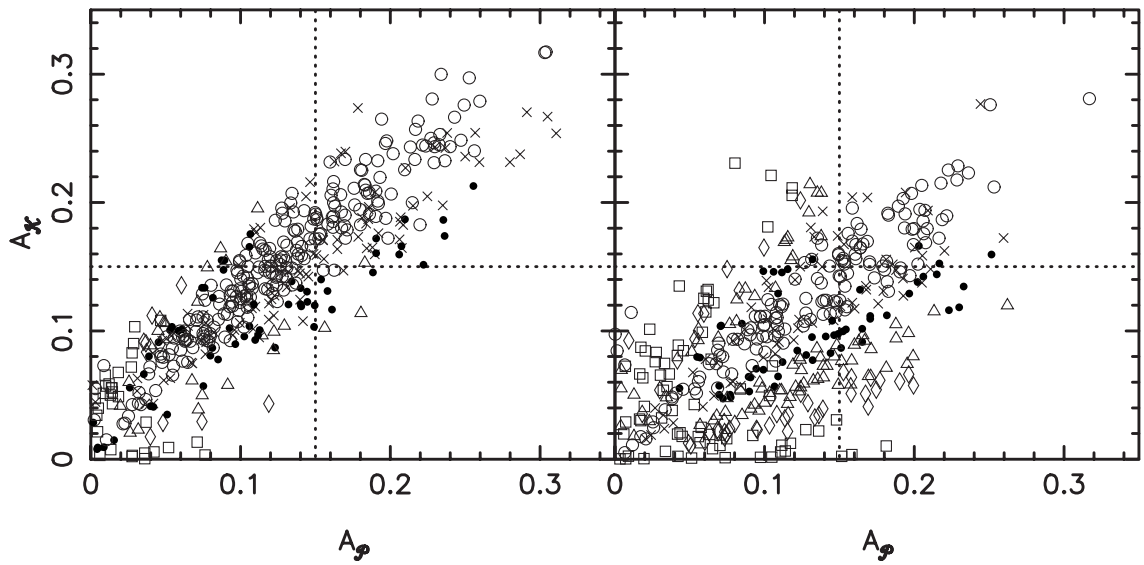

Figure 2. The fractional errors in the measurement of ΔV for a fast bar using 500 particles. The left-hand panel is for the Gaussian probability and the right-hand panel for the cosine probability. The symbols represent (absolute) errors as follows: circles $0.0 \leqslant |\delta(\Delta V)/\Delta V| < 0.2$, crosses $0.2 \leqslant |\delta(\Delta V)/\Delta V| < 0.3$, filled circles $0.3 \leqslant |\delta(\Delta V)/\Delta V| < 0.4$, triangles $0.4 \leqslant |\delta(\Delta V)/\Delta V| < 0.6$, diamonds $0.6 \leqslant |\delta(\Delta V)/\Delta V| < 0.8$ and squares $0.8 \leqslant |\delta(\Delta V)/\Delta V|$.

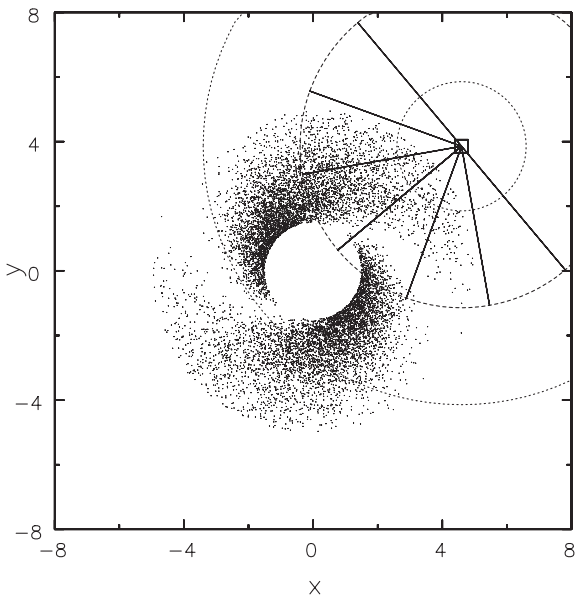

Figure 3. The simple spiral system. The 10 000 particles shown are all from the spiral component; for clarity, the axisymmetric component has not been plotted. The observer, for the orientation of Fig. 5, is marked by a square, with the line segments indicating $l = 0°$, $\pm 30°$, $\pm 60°$ and $\pm 90°$. The dashed circle then has a radius $\bar{r} = 5R_{\rm d}$ and the dotted circles have radius $\bar{r} \pm \sigma_r = 5 \pm 3R_{\rm d}$.

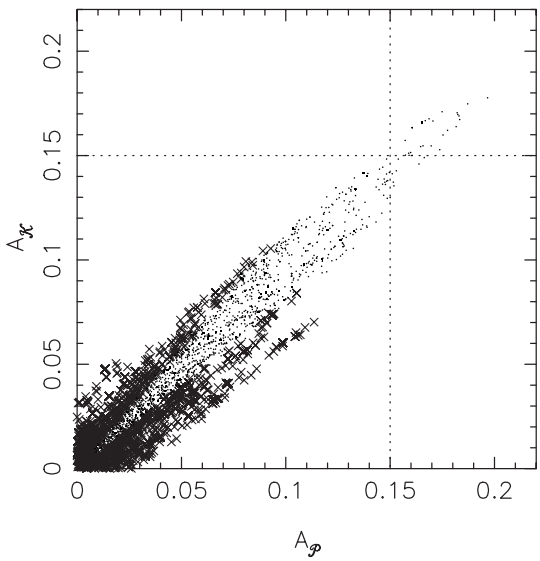

Figure 4. Errors in ΔV in the analyses of simple spiral models. The subsamples include different radial probability functions, orientations and $30° \leqslant l_0 \leqslant 45°$. Points have $|\delta(\Delta V)/\Delta V| \leqslant 20$ per cent while crosses have $|\delta(\Delta V)/\Delta V| > 20$ per cent. Clearly, in all cases where $A_{\mathcal{P}} \gtrsim 0.15$ and $A_{\mathcal{K}} \gtrsim 0.15$, the expected error in ΔV is $\lesssim 20$ per cent.

in ψ (within our range) and l_0 did not substantially change $A_{\mathcal{P}}$ and $A_{\mathcal{K}}$, and the error is not overly sensitive to variations in these parameters. For the cosine probability distribution, $A_{\mathcal{P}}$ and $A_{\mathcal{K}}$ were insensitive to variations in all three parameters. It is particularly reassuring that the errors do not depend on l_0, provided that the bar is inside l_0.

3.2 Spiral pattern speeds

Stationary spiral models based on density wave theory are somewhat harder to construct. Because we have already demonstrated that the TW method works well for bars, which have larger non-circular motions than do spirals, a crude spiral model with purely circular orbits suffices for a spiral test. We therefore generated an exponential disc in the radial range $1.5R_{\rm d} \leqslant r \leqslant 5R_{\rm d}$, consisting of two components, an axisymmetric component with particles on circular orbits at velocity 2.5 in some arbitrary units and a material (rather than wave) spiral part, which consisted of particles on circular orbits with constant $\Omega_{\rm p} = 1$. The spiral density varied tangentially as $1 + \cos 2(\theta - \theta_0)$, where $\theta_0 = \Omega_{\rm p} t - \ln(r) \cot \gamma$, to produce two-armed logarithmic spirals of pitch-angle γ, which we set to 20°. Both components were modelled by a Gaussian vertically, with equal scaleheights. The axisymmetric component accounted for 2/3 of the total mass, producing a spiral contrast

consistent with that observed in external galaxies (Rix & Zaritsky 1995). The spiral component is shown in Fig. 3.

Once we generated this system, we computed the integrals of equation (9) for a variety of orientations. In Fig. 4, we plot the errors at $l_0 \geqslant 30°$ as before for the bar; in all cases the error is $\lesssim 20$ per cent when $A_{\mathcal{P}} \gtrsim 0.15$ and $A_{\mathcal{K}} \gtrsim 0.15$. Because our rather crude spiral model included no random motions, we expect that more realistic errors will resemble those we found for the bar, provided signals are large.

Our analysis of one orientation on a sample of 500 stars, selected with a Gaussian probability of $\bar{r} = 5R_{\rm d}$ and $\sigma_r = 3R_{\rm d}$, is shown in Fig. 5; at $l_0 = 45°$, the error on ΔV is 7.5 per cent for this case. Note that $A_{\mathcal{P}}$ and $A_{\mathcal{K}}$ are both less than 0.2 at $l_0 = 45°$, which is smaller than the signal seen in the OH/IR stars (Section 5). The results for this orientation bear a striking resemblance to those of the OH/IR stars discussed in Section 5.1.

We ran a variety of additional tests of the TW method on our simple spiral system, with varying system orientation, radial probability function, number of particles selected, and reduced spiral mass fraction. These cases gave results consistent with those shown in Fig. 4; unsurprisingly, we found that the error decreases as the number of particles is increased.

3.3 Synthesis of the tests

We have shown that, for 500 stars, we expect to be able to measure ΔV with average errors of ~ 17 per cent, and always less than 40 per cent, for either a bar or a spiral, provided that signals are large ($A_{\mathcal{P}}$ and $A_{\mathcal{K}} \gtrsim 0.15$). Furthermore, we found that limiting l_0 does not lead to large errors, provided that the full non-axisymmetric structure is included.

In addition to the tests described above, we also experimented with other parameters, with results generally in agreement with those presented here. The notable exception was the case of discontinuous $f(r)$ values, which gave large errors. Such errors can be understood in terms of noisy surface terms in the integrals. Lacking distance information, $f(r)$ can only be a continuous function, corresponding to the detection probability.

4 THE OH/IR STAR CATALOGUE

4.1 OH/IR stars

OH/IR stars are oxygen-rich, cool AGB stars in the superwind phase (Renzini 1981) with typical $\dot{M} \sim 10^{-5}\,{\rm M}_{\odot}\,{\rm yr}^{-1}$. The wind outflow velocity, $V_{\rm e}$, is ~ 10–$30\,{\rm km\,s}^{-1}$, with $V_{\rm e}$ larger in the more massive (younger) OH/IR stars. The mass-loss rate is large compared to the stellar mass (typically, 1 to 6 $\rm M_{\odot}$) and the superwind phase is therefore believed to be very short-lived; $\sim 10^5$–$10^6\,{\rm yr}$ (Whitelock & Feast 1993). Thus they are rare objects. On the other hand, they are old objects, with ages ~ 1–$8\,{\rm Gyr}$, and are therefore dynamically relatively relaxed. The dusty circumstellar envelope which forms from the outflowing material absorbs the stellar radiation and re-emits it in the infrared, pumping OH masers (Elitzur, Goldreich & Scoville 1976) in the process. In optically thick envelopes, the strongest line of this maser is at 1612.23 MHz, which is conveniently insensitive to interstellar

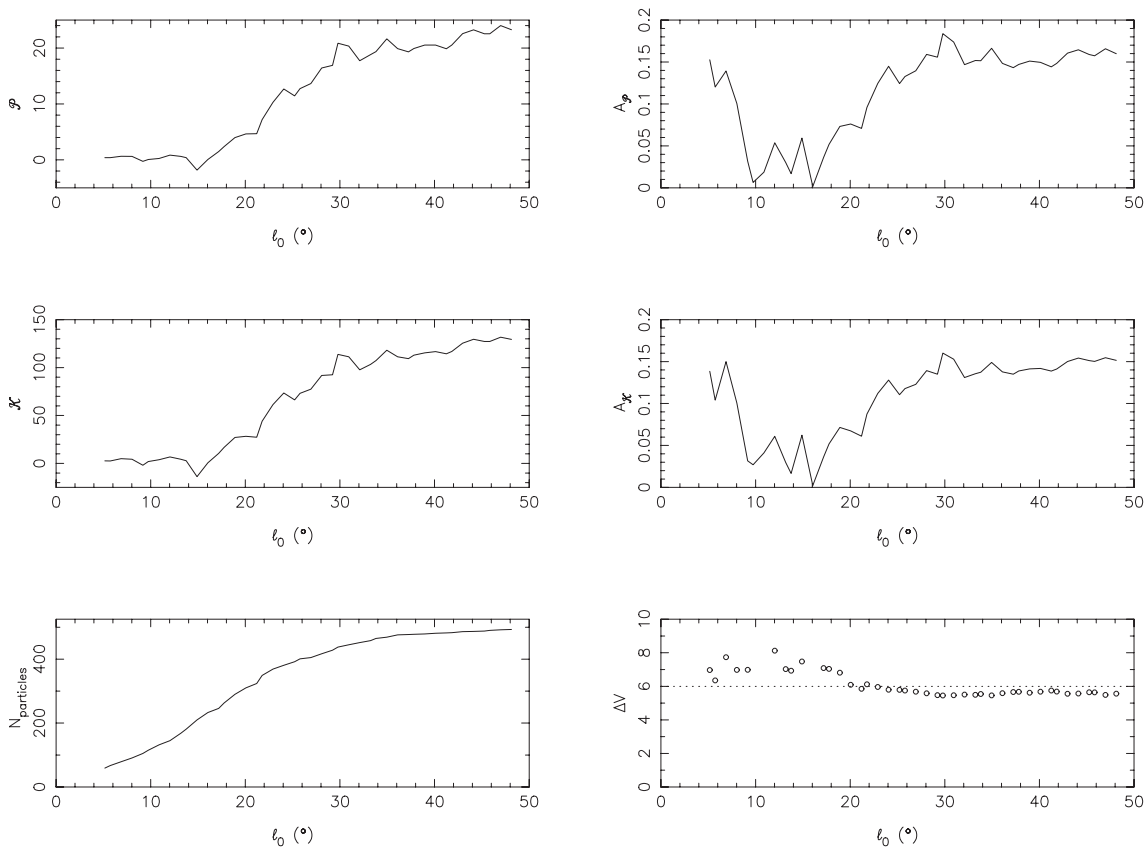

Figure 5. The results of analysis with 500 particles drawn from the simple spiral model in the orientation of Fig. 3. In the top row are $\mathcal{P}$ and $A_{\mathcal{P}}$, in the middle row $\mathcal{K}$ and $A_{\mathcal{K}}$, and in the bottom row is shown the number of particles, $N_{\rm particles}$, and ΔV obtained. The correct value of ΔV is shown by the dotted line.

extinction. The Doppler-shifted profile from the front and back of the thin OH shell permits easy identification of OH/IR stars, which makes possible an unbiased survey of these objects, tracing the kinematics of the inner MWG. A full review of the properties of OH/IR stars can be found in Habing (1996).

4.2 The ATCA/VLA OH 1612-MHz survey

We have used the data from the OH/IR star catalogue to search for pattern speeds in the inner MWG. The data were obtained in three surveys: the ATCA-bulge and ATCA-disc surveys (Sevenster et al. 1997a,b) at the Australia Telescope Compact Array (ATCA), covering $-45.25° \leqslant l \leqslant 10.25°$, $|b| \leqslant 3.25°$, and the VLA-disc survey (Sevenster et al. 2001) at the Very Large Array (VLA), covering $4.75° \leqslant l \leqslant 45.25°$, $|b| \leqslant 3.25°$. The ATCA region was covered uniformly with 1449 pointings. On the other hand, only 92 per cent of the VLA region was surveyed, with 965 pointings out of 1053 giving useful data. In all, the surveys produced 793 detections. The ATCA-bulge and VLA-disc surveys have a small overlap region ($4.75° \leqslant l \leqslant 10.25°$). In this overlap region, 27 sources were observed in both surveys, thus only 766 independent sources were found. However, the overlap region also included detections in either only the VLA-disc or only the ATCA-bulge survey, which is, in part, a manifestation of the intrinsic variability of OH/IR stars.

Details of the reduction technique for the three surveys are contained in Sevenster et al. (1997a,b) and Sevenster et al. (2001). Of the 793 detections, no outflow velocity was measured in 105 sources. Because such objects can be supergiants or even star-forming regions, rather than OH/IR stars, and don't have well-determined velocities, we have excluded them from our analysis.

The use of two separate instruments for compiling the catalogue introduces a systematic difference in the completenesses of the two sides of the MWG. We corrected for the (empirically determined) completenesses, rewriting equation (8):

$$\Delta V = \frac{\sum_p \left(C_p^{-1} \sum_{s\in p} v_{r,s} \right)}{\sum_p \left(C_p^{-1} \sum_{s\in p} \sin l_s \cos b_s \right)}, \tag{16}$$

where $\sum_p$ is a sum over pointings, $\sum_{s\in p}$ is a sum over stars detected in pointing p and C_p is the completeness of pointing p. The completenesses consist of two terms: $C_p = C_{p,a} C_{p,n}$. The first term, $C_{p,a}$, is a measure of the fraction of the surveyed area that is within some threshold radius. For this purpose, all VLA pointings, including the missing ones, were treated identically, and the $C_{p,a}$ values were calculated by Monte Carlo integration. The threshold radii were set by requiring a constant primary beam response (PBR) threshold, equal in both telescopes, for each pointing centre. The PBR of the two instruments is shown in Fig. 6; Table 1 lists several PBR levels, with the corresponding offset radii and values of $C_{p,a}$.

The second term, $C_{p,n}$, is a completeness due to the noise level, and varies from pointing to pointing. The $C_{p,n}$ values were obtained from the observed OH/IR star cumulative flux density distribution, N_*, shown in Fig. 7, as the fraction of stars between the flux limits which are brighter than the detection threshold of each pointing. This is computed in the following way:

$$C_{p,n} = \frac{N_*[\max(f_{\min}, N_s\sigma_p) \leqslant f \leqslant f_{\max}]}{N_*(f_{\min} \leqslant f \leqslant f_{\max})}. \tag{17}$$

Here, $f_{\min}$ and $f_{\max}$ are the flux density limits we use, σ_p is the noise in pointing p and N_s is the multiplicative detection threshold ($N_s = 7, 4, 6$, empirically determined for VLA-disc, ATCA-bulge, ATCA-disc respectively). We chose $f_{\min} = 0.16$ Jy, as this is the highest of the lower absolute detection thresholds of the three surveys, and no upper limit on f. The noise level was more variable in the VLA-disc survey then in the ATCA surveys. In Fig. 8, we plot the resulting distribution of the $C_{p,n}$ values.

The three surveys had different velocity coverages: the ATCA-bulge survey covered $-280 \leqslant v_r \leqslant 300\,\mathrm{km\,s^{-1}}$, the ATCA-disc survey covered $-295 \leqslant v_r \leqslant 379\,\mathrm{km\,s^{-1}}$, while the VLA-disc survey had full coverage in the range $-200 \leqslant v_r \leqslant 210\,\mathrm{km\,s^{-1}}$. Thus the three surveys had full *common* velocity coverage from -200 to $200\,\mathrm{km\,s^{-1}}$. A considerable number of detections were obtained at $|v_r| > 200\,\mathrm{km\,s^{-1}}$, but these are mostly at $|l| \leqslant 5°$. One detection was obtained at $270\,\mathrm{km\,s^{-1}}$ in the ATCA-disc survey, but as this turned out to be a single-peaked object anyway, it was excluded from our analysis.

Typical errors in positions are $\leqslant 1$ arcsec for the ATCA surveys and 2 arcsec for VLA-disc survey. These position errors introduce negligible errors in the value of ΔV, as can be appreciated from equation (8). The velocity errors are of order $1\,\mathrm{km\,s^{-1}}$ for the ATCA surveys, and $2.5\,\mathrm{km\,s^{-1}}$ for the VLA-disc survey. The velocity errors produce larger errors in ΔV, although, as will be seen below, these are still quite small.

The values of v_r reported in Sevenster et al. (1997a,b, 2001) included a correction for an assumed solar peculiar motion of $19.7\,\mathrm{km\,s^{-1}}$ towards $\mathrm{RA} = 18^{\mathrm{h}}07^{\mathrm{m}}50\overset{\mathrm{s}}{.}3$, $\mathrm{Dec} = +30°00'52''$ (J2000.0). For this study, we are adopting the solar peculiar motion found by Dehnen & Binney (1998); we have therefore had to transform from the Sevenster et al. frame to that of Dehnen & Binney.

The mass, and therefore age and luminosity, of OH/IR stars correlate with V_e. For example, Sevenster (2002) finds that OH/IR stars with $V_e = 13$ (17.5) $\mathrm{km\,s^{-1}}$ have a mass of roughly 1.7 (4) $\mathrm{M}_\odot$ and therefore an age of 1.8 (0.2) Gyr. We can anticipate, therefore, that we will need to make cuts on V_e. However, the V_e values have been measured in units of half the channel widths ($2.27\,\mathrm{km\,s^{-1}}$ for the VLA-disc survey, and $1.46\,\mathrm{km\,s^{-1}}$ for the ATCA surveys). To compensate for this effective binning, we have randomized the outflow velocities within each bin. We did this in a

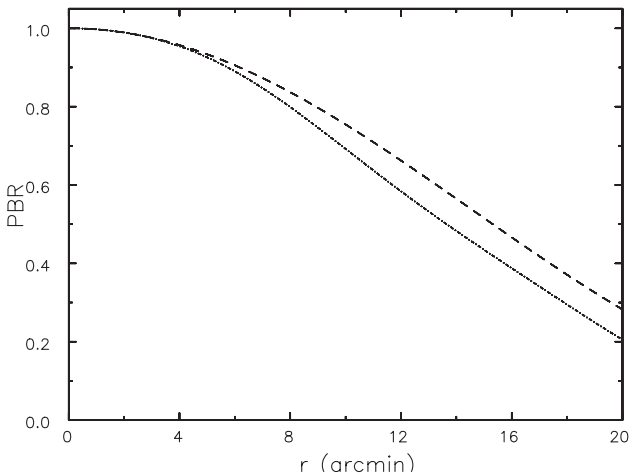

Figure 6. The PBR for the two instruments used in the OH/IR survey. The dashed (dot-dashed) line is the PBR for the ATCA (VLA).

Table 1. The VLA and ATCA maximum offsets and the resulting values of $C_{p,a}$ for various PBR levels.

PBR level	VLA offset (arcmin)	$C_{p,a}$ (VLA)	ATCA offset (arcmin)	$C_{p,a}$ (ATCA)
0.5	13.6	0.656	15.3	0.812
0.6	11.7	0.489	13.3	0.623
0.7	9.9	0.347	11.2	0.450

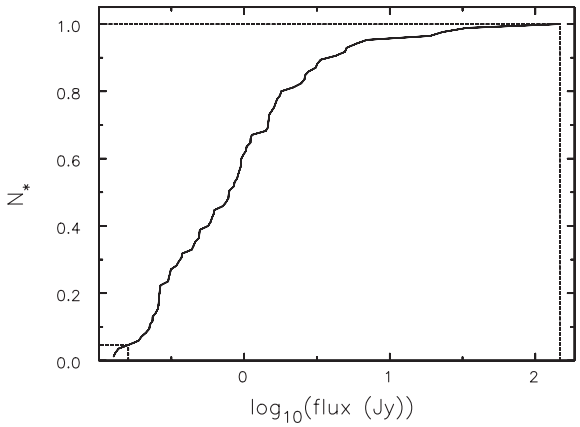

Figure 7. The cumulative flux distribution of OH/IR stars in the ATCA/VLA OH 1612-MHz survey. We used this flux distribution, defined from all sources with highest peak observed at PBR >0.8, to compute the noise completenesses, $C_{p,n}$ of the pointings. The lower limit is at 0.16 Jy while the upper limit is here set at the brightest observed OH/IR star (147.6 Jy).

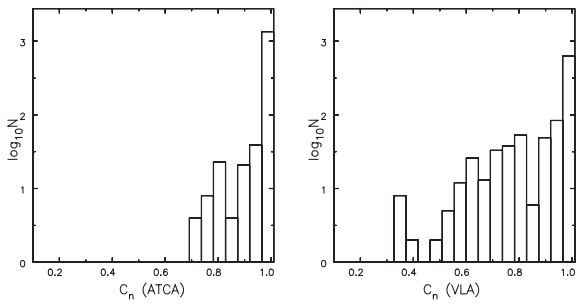

Figure 8. The distribution of the $C_{p,n}$ values. On the left are shown the ATCA pointings, and on the right are the VLA pointings. The effect of the higher noise level in the VLA-disc survey is easily apparent.

number of ways with similar results once random re-samplings were performed; we have therefore relied on the simplest approach, namely to add to each V_e a random value distributed uniformly between -1.2 and $1.2\,\mathrm{km\,s^{-1}}$.

The luminosity, L_*, of OH/IR stars increases with V_e: simple models predict $V_e^4 \propto L_*$, while more sophisticated models predict $V_e^{3.3} \propto L_*$ (Habing, Tignon & Tielens 1994). Thus a flux density-limited sample will probe to different distances for different V_e. In Fig. 9 we plot the maximum longitude, $|l|_{max}$, of OH/IR stars versus V_e, from which it can be seen that OH/IR stars of low V_e are found only at small $|l|$. We interpret this as resulting from the ATCA/VLA OH 1612-MHz survey being able to detect only the very nearest faint OH/IR stars of a distribution ending inside the solar circle. For the faint stars, the effect of small-scale number density fluctuations is large, both because only a small portion of the disc is seen and because the number of such stars is low. We have therefore chosen to exclude all OH/IR stars with $V_e < 10\,\mathrm{km\,s^{-1}}$.

The TW method requires a sample of stars that form a relatively relaxed population; a convenient cut-off criterion would be at least 2.5 rotations at 6 kpc. This requires ages greater than 0.5 Gyr, or $V_e \leqslant 16\,\mathrm{km\,s^{-1}}$. However, because we have had to randomize the outflow velocities we used only stars with $V_e \leqslant 15\,\mathrm{km\,s^{-1}}$, to minimize contamination by very young stars. Thus our final range in outflow velocities is $10 \leqslant V_e \leqslant 15\,\mathrm{km\,s^{-1}}$, which is expected to cover a distance range of from 4 to 10 kpc from the Sun. The lower limit removes roughly 10 per cent of stars from the sample, while the upper limit removes a further 35 per cent.

5 RESULTS

5.1 A pattern speed in the disc

We computed $\mathcal{P}$, $\mathcal{K}$, $A_{\mathcal{P}}$ and $A_{\mathcal{K}}$ for $5^\circ \leqslant l_0 \leqslant 45^\circ$ in steps of 1°. We set $f_{\min} = 0.16$ Jy, $PBR = 0.5$ and excluded OH/IR stars with $|v_r| > 280\,\mathrm{km\,s^{-1}}$. We tried both using the ATCA and the VLA in the overlap region. At each l_0, the values reflect averages over 100 Monte Carlo experiments containing slightly different samples. In these experiments, the V_e's were randomized in their bins (as described above) and Gaussian random errors of $\sigma_v = 5\,\mathrm{km\,s^{-1}}$ added to the radial velocities. These results are presented in Fig. 10. It is immediately clear that there is effectively no difference between using the ATCA or the VLA in the overlap region. Therefore, because the ATCA survey tends to be less noisy, we use it from here on. For $l_0 \leqslant 25^\circ$, both $\mathcal{P}$ and $\mathcal{K}$ are small and roughly constant, while $A_{\mathcal{P}}$ and $A_{\mathcal{K}}$ are noisy, suggesting they are strongly affected by Poisson noise. In the range $25^\circ \leqslant l_0 \leqslant 33^\circ$, $\mathcal{P}$, $\mathcal{K}$, $A_{\mathcal{P}}$ and $A_{\mathcal{K}}$ all grow very rapidly. At $l_0 \simeq 33^\circ$, there is a sudden change in the slope of the number of included stars, which is associated with almost constant $\mathcal{P}$, $\mathcal{K}$, $A_{\mathcal{P}}$ and $A_{\mathcal{K}}$ at $l_0 \geqslant 33^\circ$. In this region, both $A_{\mathcal{P}}$ and $A_{\mathcal{K}}$ are $\gtrsim 0.15$, which our simple tests of Section 3 suggest is large enough for moderate error levels. Averaging over $l_0 \geqslant 35^\circ$, we obtain $\mathcal{K}/\mathcal{P} = 263 \pm 44\,\mathrm{km\,s^{-1}}$, where we have used one half of the difference between the maximum and minimum value for the error estimate as the values of $\mathcal{K}/\mathcal{P}$ at different l_0 are not independent. Then, if $u_{LSR} = 0$, $R_0 = 8$ kpc and $V_{LSR} = 220\,\mathrm{km\,s^{-1}}$ (which we assume for the remainder of this paper except where otherwise noted), $\Omega_p = 60 \pm 6\,\mathrm{km\,s^{-1}\,kpc^{-1}}$.

Another way of presenting the data of Fig. 10 is shown in Fig. 11, where we plot the same data for $l_0 = 45^\circ$ but without the averaging of the various values of $\mathcal{K}$ and $\mathcal{P}$ resulting from the Monte Carlo reshufflings of V_e. In the upper panel of this figure, we also plot lines of constant Ω_p (40, 50, 60, 70 and $80\,\mathrm{km\,s^{-1}\,kpc^{-1}}$) assuming $R_0 = 8$ kpc and $V_{LSR} = 220\,\mathrm{km\,s^{-1}}$ for $u_{LSR} = 0$ and for $u_{LSR} = 5\,\mathrm{km\,s^{-1}}$. For the $u_{LSR} = 0$ case, the various re-samplings have average $\Omega_p = 57\,\mathrm{km\,s^{-1}\,kpc^{-1}}$, while in the case of $u_{LSR} = 5\,\mathrm{km\,s^{-1}}$, average $\Omega_p = 45\,\mathrm{km\,s^{-1}\,kpc^{-1}}$, graphically demonstrating the sensitivity of the value of Ω_p obtained to a small radial LSR

motion. The bottom panel also shows the effect of varying $V_{\rm LSR}$ and R_0, demonstrating that $\Omega_{\rm p}$ increases with decreasing R_0 and/or increasing $V_{\rm LSR}$. However, we will not be concerned here with errors in $V_{\rm LSR}$, R_0 and $u_{\rm LSR}$; $V_{\rm LSR}$ enters only in the ratio $V_{\rm LSR}/R_0$, which has been determined to 10 per cent accuracy, R_0 is determined to even higher accuracy, while the effect of $u_{\rm LSR}$ is considered in Section 5.4. Note that the value of ΔV obtained this way is slightly different from that obtained by averaging over l_0; because the values of ΔV at different l_0 are not independent, we quote values of ΔV and $\Omega_{\rm p}$ based on $l_0 = 45°$ only from now on.

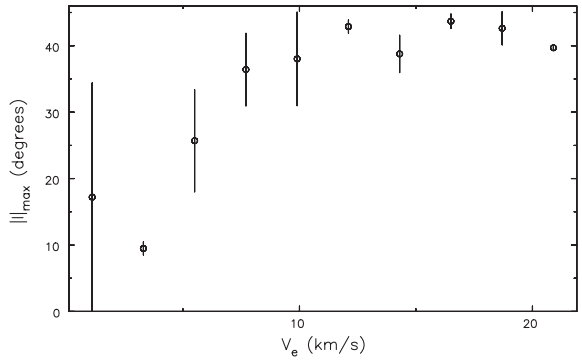

Figure 9. The dependence of $|l|_{\rm max}$ on $V_{\rm e}$, showing that only the nearest of the low $V_{\rm e}$ OH/IR stars are visible in the survey. From this figure, we conservatively estimate that only at $V_{\rm e} \geqslant 10\,{\rm km\,s^{-1}}$ are stars visible throughout the survey region ($|l| \leqslant 45°$). Each point is the average of the positive and negative l, while the error bars are defined as half the difference.

5.2 Is it real?

Before proceeding further, we present evidence that the signal we have measured is real, and not a result of a systematic error in either our analysis or the OH/IR star surveys. As $\mathcal{K}$ and $\mathcal{P}$ measure differences, any systematic error in our calculated completenesses of the VLA or ATCA survey will be amplified into a signal. Several reasons lead us to believe that this has not happened. First, the signals of Fig. 10 first become evident at a very clear region in the disc, which is well correlated with an observed structure. In Fig. 12, we present contour maps of the surface density of OH/IR stars in the survey. These clearly show the presence of very significant overdensities localized at $l \simeq 25°$ and $l \simeq 32°$.

While there are roughly equal number of stars at positive and negative l, (*despite* the missing pointings, smaller PBHW and greater noise in the VLA survey), for $25° < |l| < 33°$, there are 13 OH/IR stars at negative l and 24 at positive l, which has less than 10 per cent probability, even without taking the lower VLA detection probability into account. Thus, when all the C_p values are set to 1 (i.e. when no completeness corrections are included), the

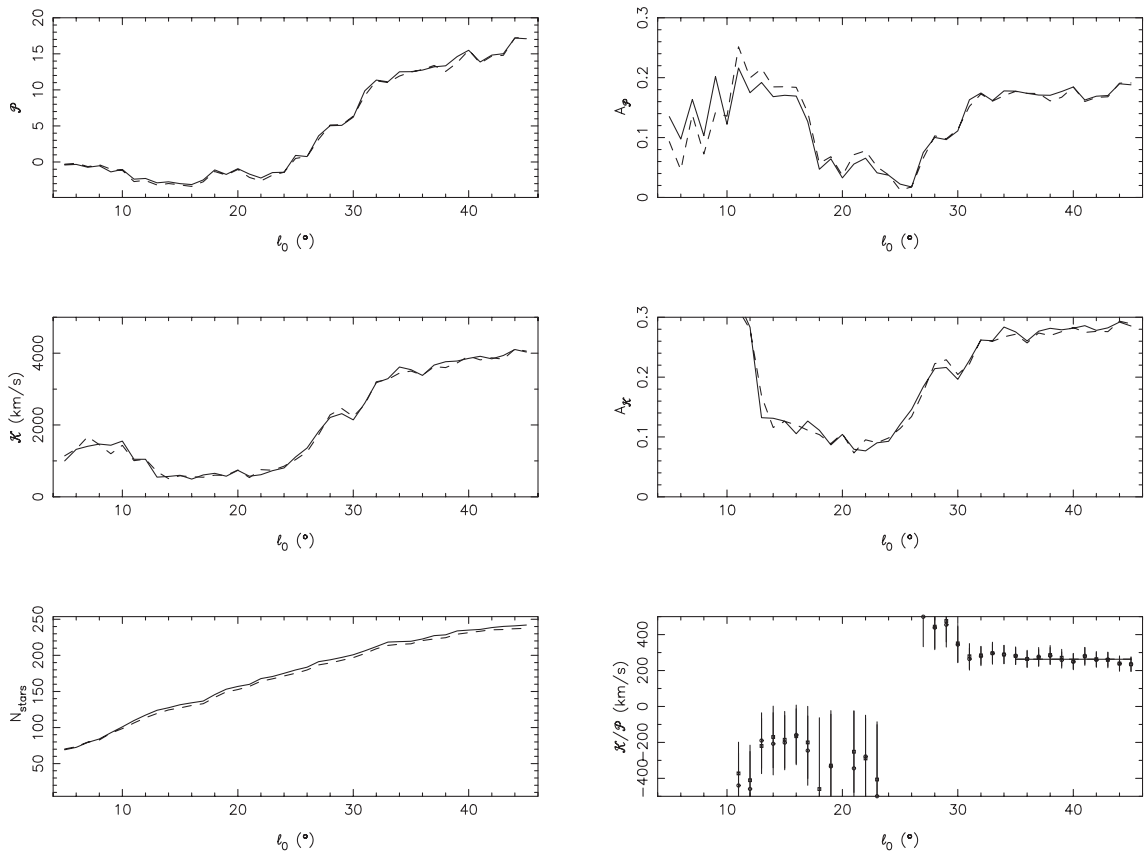

Figure 10. The TW analysis for the OH/IR stars as functions of l_0. In the top row are $\mathcal{P}$ and $A_{\mathcal{P}}$, in the middle row $\mathcal{K}$ and $A_{\mathcal{K}}$, and in the bottom row is shown the number of stars, $N_{\rm stars}$, and the resulting $\mathcal{K}/\mathcal{P}$. In all panels, the solid line corresponds to using the ATCA survey in the overlap region, while the dashed line shows the result of using the VLA survey. In the bottom right-hand panel, circles (squares) are for the ATCA (VLA) survey, and the horizontal lines indicate the value of $\mathcal{K}/\mathcal{P}$ obtained by averaging results at $l_0 \geqslant 35°$. The values of $\mathcal{K}$ and the (1σ) error bars on $\mathcal{K}/\mathcal{P}$ were obtained from 100 Monte Carlo iterations as described in the text.

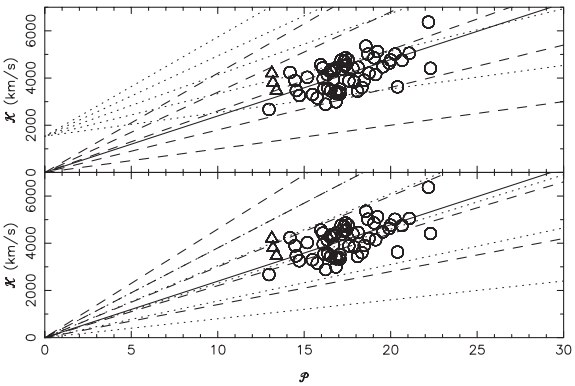

Figure 11. The values of $\mathcal{K}$ and $\mathcal{P}$ at $l_0 = 45°$ with bounds $10 \leqslant V_e \leqslant 15\,\mathrm{km\,s^{-1}}$ after reshuffling the V_e's. Each point represents a different reshuffling. Circles have $A_\mathcal{P} \geqslant 0.15$ and $A_\mathcal{K} \geqslant 0.15$, while triangles have either $A_\mathcal{P}$ or $A_\mathcal{K}$ or both less than 0.15. In the top panel, the dashed lines and dotted lines have $\Omega_p = 40$, 50, 60, 70 and $80\,\mathrm{km\,s^{-1}\,kpc^{-1}}$ (in order of increasing slope) assuming $R_0 = 8\,\mathrm{kpc}$ and $V_{LSR} = 220\,\mathrm{km\,s^{-1}}$. The dashed lines assume $u_{LSR} = 0$, while $u_{LSR} = 5\,\mathrm{km\,s^{-1}}$ for the dotted lines. The solid line (in both panels) is the average $\Omega_p = 57\,\mathrm{km\,s^{-1}\,kpc^{-1}}$. In the bottom panel, we show the effect of changing V_{LSR} to $180\,\mathrm{km\,s^{-1}}$ (dashed lines) and R_0 to 7.5 kpc (dotted lines).

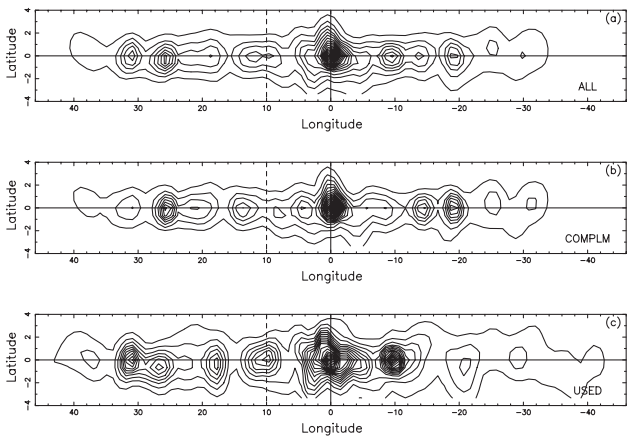

Figure 12. The surface density of OH/IR stars detected in the surveys. Adaptive smoothing has been used. The surface density has not been corrected for differences in the detection efficiencies between the ATCA ($-45° \leqslant l \leqslant 10.25°$) and the VLA ($10.25° \leqslant l \leqslant 45°$). Therefore the two sides of the plot (separated by the vertical dashed line) need to be considered separately. Note the very strong overdensities at $25° \lesssim l \lesssim 32°$. The bottom panel shows the sample of OH/IR stars used in our analysis.

qualitative behaviour of $\mathcal{P}$, $\mathcal{K}$, $A_\mathcal{P}$ and $A_\mathcal{K}$ is unchanged, although, as is to be expected, signals are then smaller.

Systematic errors in the completenesses are not likely to be the source of this signal. Suppose errors of the form $C'_{ATCA} = C_{ATCA}(1 + \delta C_{ATCA})$ and/or $C'_{VLA} = C_{VLA}(1 + \delta C_{VLA})$ were present, and suppose further that the OH/IR stars sample only an axisymmetric part of the disc. It is then easy to show that $\delta C_{VLA} - \delta C_{ATCA} \simeq \mathcal{P}/\mathcal{P}_-$ which is approximately equal to $-17/35$ in our case. Because the noise errors are random, such a large systematic error would have to be in the values of the areal completenesses, which corresponds to roughly an overestimate (underestimate) by ~ 20 per cent in the radius at any given PBR for the ATCA (VLA). Such a large error is impossible since the PBR of both instruments is well determined. A systematic effect might be introduced by the different channel widths of the VLA and the ATCA, but the similarity of the flux density distributions between the VLA and the ATCA side suggests that, at most, this is a 10 per cent effect. Furthermore, this effect acts to underestimate the flux density of the sources detected by the VLA, so that f_{min} would remove from our sample more VLA stars than ATCA stars, which would make $\mathcal{P}$ negative, which is the opposite sign from what we found.

Further evidence that the signal of Fig. 10 is real comes from the dependence of the signal on b. We explored the effects of limits in b, finding that most of the non-axisymmetric signal comes from very close to the MWG plane, with little signal at $|b| \geqslant 1°$ (which divides our sample of OH/IR stars into two roughly equal parts). This is unsurprising for a disc population: at 6 kpc, 1° corresponds to roughly the disc scaleheight. We found considerable fluctuations in the value of $\mathcal{K}/\mathcal{P}$ at $l_0 \geqslant 35°$ obtained from $|b| \geqslant 1°$, reinforcing the impression that the settling of $\mathcal{K}/\mathcal{P}$ in the previous experiments is not caused by systematic errors, e.g. in the completenesses.

All these facts make it likely, therefore, that the signal is intrinsic to the sample. Finally, it is perhaps worth drawing attention to the suggestive similarity between Fig. 5 and Fig. 10.

Although the derived value of $\mathcal{K}/\mathcal{P}$ is nearly constant in the range $35° \leqslant l_0 \leqslant 45°$, we cannot completely exclude that extending the survey to larger l_0 would not lead to a different $\mathcal{K}/\mathcal{P}$. However, the density of OH/IR stars is decreasing rapidly at $l_0 = 45°$: an extrapolation of the binned surface density suggests that their surface density will vanish at around $l_0 \simeq 60°$, as is also suggested by the dynamical models of Sevenster et al. (2000). Observationally, Le Squeren et al. (1992) found that the distribution of OH/IR stars is concentrated inside $|l| \leqslant 70°$, with only roughly 15 per cent of sources outside this range. Physically, this steep drop-off is the result of a metallicity gradient in the MWG disc: at the lower metallicities typical of the outer disc, AGB stars are more likely to evolve into carbon stars. Thus, even if there is still non-axisymmetric structure outside $l = \pm 45°$, it is not likely to change the derived value of $\mathcal{K}/\mathcal{P}$ for the OH/IR population very significantly.

5.3 Missing pointings and radial velocities

The error introduced by the missing VLA pointings is systematic in $\mathcal{K}$ and $\mathcal{P}$, in that it always reduces the VLA (i.e. positive) contribution to these terms; however, the sign of the resulting change in $\mathcal{K}/\mathcal{P}$ is not obvious. Of 88 missing pointings, 18 are in the overlap region. In general, therefore, we chose to use the ATCA pointings in the overlap region, to minimize the effect of missing pointings. To estimate the effect of the remaining missing pointings (70 of 88), we tried to reconstruct the missing pointings by reflection about the mid-plane where possible (49 pointings). Where this was not possible (21 pointings), we have simply averaged the value in the four nearest pointings, or the subset of them which were not themselves missing pointings. With these changes but all else as before, $\mathcal{P}$, $\mathcal{K}$, $A_\mathcal{P}$ and $A_\mathcal{K}$ increase somewhat, but $\mathcal{K}/\mathcal{P}$ changes to $239 \pm 30\,\mathrm{km\,s^{-1}}$, which is not significantly different from our previous values. The reason for this robustness to missing pointings can be understood by comparing the number of pointings and of OH/IR stars. Our sample contains 73 OH/IR stars detected in 840 good VLA pointings. With these probabilities, we estimate that $\lesssim 70 \times 0.09 \sim 6$ OH/IR stars have been missed because of missing VLA pointings not in the ATCA overlap region.

As a result of observational constraints, we considered only OH/IR stars with $|v_r| \leqslant 280\,\mathrm{km\,s^{-1}}$. We experimented with reducing the maximum $|v_r|$ further to test how our limit might have

affected our value of $\mathcal{K}/\mathcal{P}$. Radial velocities this large are expected to occur only in the bulge region, and indeed, the biggest relative changes in $\mathcal{K}$ were at small l_0, but these propagated to small changes in $\mathcal{K}$ at large l_0. It is only at $|v_r| \leqslant 250\,\mathrm{km\,s^{-1}}$ that stars begin to leave the sample, and $\mathcal{K}/\mathcal{P}$ decreases slowly for smaller maximum $|v_r|$, reaching $229 \pm 40\,\mathrm{km\,s^{-1}}$ at $|v_r| \leqslant 200\,\mathrm{km\,s^{-1}}$, which is within 1σ of the value for the full sample. We therefore conclude that it is unlikely that our modest cut in $|v_r|$ has resulted in a large systematic error in $\mathcal{K}/\mathcal{P}$.

5.4 Radial motion of the LSR

A non-zero radial velocity of the LSR, u_{LSR}, cannot be excluded. For our OH/IR star sample, $\mathcal{S}/\mathcal{P} \simeq 18$. Thus even quite a small u_{LSR} will drastically alter the value of ΔV: if $u_{\mathrm{LSR}} \simeq 14\,\mathrm{km\,s^{-1}}$, then ΔV changes by 100 per cent. An accurate measurement of u_{LSR} is therefore needed.

Averaging the 197 OH/IR stars at $-10^\circ \leqslant l \leqslant 10^\circ$ (i.e. the ATCA-bulge survey), we estimated $u_{\mathrm{LSR}} = +2.7 \pm 6.8\,\mathrm{km\,s^{-1}}$ (the plus sign indicating that the motion is away from the Galactic centre). Similarly, Kuijken & Tremaine (1994) used a variety of tracers (OH/IR stars, globular clusters, high-velocity stars, planetary nebulae, etc.) to obtain $u_{\mathrm{LSR}} = -1 \pm 9\,\mathrm{km\,s^{-1}}$. Perhaps the best constraint on u_{LSR} is that of Radhakrishnan & Sarma (1980), who showed that the main component in the H I absorption spectrum of Sgr A has a mean line-of-sight velocity $\bar{v}_R = -0.23 \pm 0.06\,\mathrm{km\,s^{-1}}$. As this absorbing material is presumably outside the inner region of the MWG and within 6–7 kpc from the Sun, this means that a wide band of material is moving at a common radial velocity. While it is possible to construct models in which $\mathrm{d}\bar{v}_R/\mathrm{d}R$ is zero but with non-zero u_{LSR} (e.g. Blitz & Spergel 1991), the most natural explanation is that u_{LSR} is zero to this level; if $u_{\mathrm{LSR}} = -0.23\,\mathrm{km\,s^{-1}}$, this changes ΔV by $-4\,\mathrm{km\,s^{-1}}$.

5.5 Sampling experiments and error estimates

We now estimate the errors arising from sampling, which should be the largest source of errors for our small sample. We do this by re-sampling the data; however, because arbitrary resamplings will increase the noise, we first sorted the OH/IR stars by V_{e}, then took subsamples of 220, 230 and 240 consecutive stars. At each subsample size, we generated 1000 different reshufflings of the V_{e} values (because we always used $10 \leqslant V_{\mathrm{e}} \leqslant 15\,\mathrm{km\,s^{-1}}$, the number of combinations of OH/IR stars, and therefore the number of different values of $\mathcal{K}$ versus $\mathcal{P}$, is smaller than 1000). The results are presented in Fig. 13, which shows clearly that there is quite a fair amount of scatter in the values of $\mathcal{K}$ and $\mathcal{P}$. The median value of $\Delta V = 252 \pm 41\,\mathrm{km\,s^{-1}}$; this corresponds to $\Omega_{\mathrm{p}} = 59 \pm 5\,\mathrm{km\,s^{-1}\,kpc^{-1}}$. Therefore, as an estimate of the sampling noise, we adopt $5\,\mathrm{km\,s^{-1}\,kpc^{-1}}$.

The error estimate on ΔV from sampling is consistent with the results we found in Section 3, and with the estimate based on variations in l_0. We further test this error estimate by taking a subsample of $PBR = 0.6$, which gives about 180 stars. Then the average $\Delta V = 175 \pm 23\,\mathrm{km\,s^{-1}}$, which is within 2σ of the result for the full sample. As this is an even smaller sample than our main sample, it should be even noisier than our full sample. We conclude that our sampling error estimate is reasonable. (Higher PBR levels give even smaller samples and require larger areal corrections (see Table 14), which make them too susceptible to noise. We have therefore not attempted to use PBR levels above 0.6.)

We have experimented with other subsamples; in all cases we found that the results were not statistically different from the results we presented above. However, we found that the average Ω_{p} tends to systematically increase as the upper cutoff on V_{e} is decreased. Thus, for example, we find that for $10 \leqslant V_{\mathrm{e}} \leqslant 14.5\,\mathrm{km\,s^{-1}}$ (212 stars), the average $\Omega_{\mathrm{p}} = 64\,\mathrm{km\,s^{-1}\,kpc^{-1}}$ while for $10 \leqslant V_{\mathrm{e}} \leqslant 14.0\,\mathrm{km\,s^{-1}}$ (181 stars), the average $\Omega_{\mathrm{p}} = 69\,\mathrm{km\,s^{-1}\,kpc^{-1}}$. The same trend was seen when we increased the upper V_{e} to $16\,\mathrm{km\,s^{-1}}$, although in that case we are less certain that the population is relaxed. While all these results are consistent with $59\,\mathrm{km\,s^{-1}\,kpc^{-1}}$ within 2σ, the systematic behaviour suggests that there is a systematic error, perhaps due to the population not being fully relaxed. We take as an estimate of this error $10\,\mathrm{km\,s^{-1}\,kpc^{-1}}$.

6 DISCUSSION AND CONCLUSIONS

The results of our study of the OH/IR stars in the ATCA/VLA OH 1612-MHz survey give us a pattern speed of $\Omega_{\mathrm{p}} = 59 \pm 5 \pm 10\,\mathrm{km\,s^{-1}\,kpc^{-1}}$ (internal and estimated systematic errors respectively) for $u_{\mathrm{LSR}} = 0$, $R_0 = 8\,\mathrm{kpc}$ and $V_{\mathrm{LSR}} = 220\,\mathrm{km\,s^{-1}}$. If the rotation curve stays flat between the region of the non-axisymmetry and the Sun, then the corotation radius is $3.7 \pm 0.3^{+0.8}_{-0.5}\,\mathrm{kpc}$, while the main non-axisymmetric feature in question appears to be centred at $l \sim 30^\circ$, i.e. $\sim 4.0\,\mathrm{kpc}$ if it is seen tangentially. If this is the full extent of this non-axisymmetric feature, then $\mathcal{R} = 0.9 \pm 0.1^{+0.2}_{-0.1}$, which is fast in the usual definition. However, it is possible that the feature is not being viewed tangentially and extends somewhat further out, in which case $\mathcal{R}$ would be smaller.

Which feature in the MWG disc can be responsible for the signal we have measured? While the TW method has the great advantage of being model-independent, the result is that, in the absence of distance information, it is hard to identify the feature responsible for the pattern speed measured. For such a fast feature, the MWG bar would seem to be the natural explanation. However, the longitude at which the non-axisymmetric signal peaks is somewhat larger than what present models of the MWG would have (e.g. Gerhard 2001, but see Hammersley et al. 2000, who have recently claimed evidence of a second, larger bar in the MWG).

The small latitude of the main part of the signal implies a disc source, while the large longitude suggests the signal arises mostly from spirals, particularly at the tangent point of the Scutum spiral

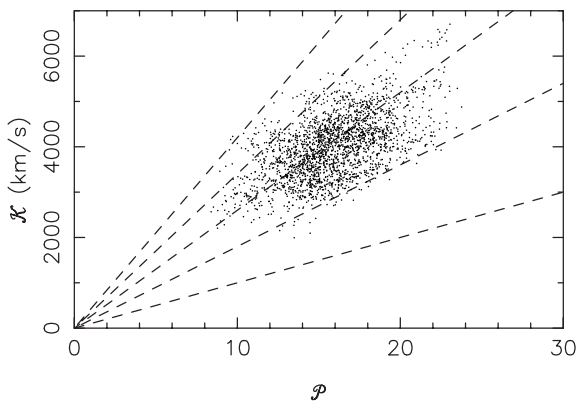

Figure 13. The distribution of values of $\mathcal{K}$ and $\mathcal{P}$ in re-sampling experiments with 220, 230 and 240 OH/IR stars. The list of stars is first sorted by V_{e}, then consecutive stars are sampled in the range $10 \leqslant V_{\mathrm{e}} \leqslant 15\,\mathrm{km\,s^{-1}}$. The dashed lines indicate $\Omega_{\mathrm{p}} = 40$, 50, 60, 70 and $80\,\mathrm{km\,s^{-1}\,kpc^{-1}}$.

arm. The high value of Ω_p and the relatively small $\mathcal{R}$ may hint at a coupling to the bar; perhaps it is even an inner ring, rather than a spiral arm. Such rings are often found in external barred galaxies (Buta 1995), and are elongated along the bar, so that they co-rotate with the bars which they contain. Such a ring has been postulated in the MWG (e.g. Sevenster & Kalnajs 2001).

The pattern speed measured must, in fact, be a density- and asymmetry-weighted average of all the non-axisymmetric structure in the survey region, which is known to include a bar, various spirals and perhaps a ring. Note that there is no evidence of substantial cancellation of $\mathcal{P}$ in Fig. 10. For various subsamples, we find some marginal evidence for multiple pattern speeds: when we divided our full sample into bright (flux density >0.854 Jy) and faint (flux density <0.854 Jy) subsamples, we found $\Omega_p = 49 \pm 6\,\mathrm{km\,s^{-1}\,kpc^{-1}}$ and $\Omega_p = 71 \pm 14\,\mathrm{km\,s^{-1}\,kpc^{-1}}$, respectively, together with some evidence of signals peaking at different l_0. As the bright (faint) subsample is, on average, expected to be closer to (further from) the Sun and further from (closer to) the Galactic centre, the lower (higher) pattern speed is not unexpected. However, these subsamples are even smaller than our already small full sample, and the differences are not statistically significant. Multiple pattern speeds can be studied better with larger samples of tracers.

6.1 Future prospects

In the future, it will be possible to improve on our measurement in a variety of ways. Our main limitation was the small sample of objects; larger samples will provide one means of improving on our measurement. At present, the ATCA/VLA OH 1612-MHz survey is the only large scale complete survey of a population satisfying the continuity equation. Kuijken & Tremaine (1991) applied the TW method to the Galactic H I, which covers the entire disc, but this is unlikely to satisfy continuity, particularly in the presence of a bar. However, systematic surveys of other populations are now in progress (e.g. planetary nebulae, Beaulieu et al. 2000; SiO masers, Deguchi, Nakashima & Balasubramanyam 2001) or planned (Honma, Kawaguchi & Sasao 2000); these may be used for similar measurements.

Accurate distance information will lead to an important refinement in the method. Future astrometric satellites, such as the European Space Agency's (ESA's) *GAIA*, will measure radial velocities together with distance. Not only will *GAIA* provide samples many orders larger than the ATCA/VLA OH 1612-MHz survey, but it will also be possible to drop the assumption of one pattern speed. Then, if the pattern speed is some function of Galactocentric radius only, we can write

$$\int \Omega_p(\rho)\mu(\rho,\psi)\cos\psi\rho^2 f(R)\,\mathrm{d}\psi\,\mathrm{d}\rho$$

$$= \int \mu(\rho,\psi)\rho v_R(\rho,\psi) f(R)\,\mathrm{d}\psi\,\mathrm{d}\rho, \qquad (18)$$

where (ρ, ψ) are Galactocentric polar coordinates, R is the usual distance from the Sun, and for simplicity we have ignored both the third dimension and LSR motion. This is a Fredholm integral equation of the first kind for the unknown function $\Omega_p(\rho)$; techniques for the solution of such equations, including numerical methods, are well established. The main difficulty with a solution of this equation probably arises in regularising the solution at helio-centric radii R at which the integrals are small or vanish, as must happen for a spiral, but a detailed discussion of these issues is beyond the scope of this paper. Such data will make it possible to test theories of spiral structure in greater detail than has been possible to now.

6.2 Conclusions

We derived a 3D version of the Tremaine–Weinberg method for the Milky Way Galaxy. The method, as developed here, is based on the assumption that the density distribution can be expressed as in equation (1). Thus we have assumed one pattern speed only; if multiple pattern speeds are present, then an average pattern speed is measured, as discussed in Section 2.3. Moreover, we have assumed that any rapidly growing structure present has low amplitude. We argued that this is likely to be the case as large amplitude features cannot sustain large growth for long.

We tested the method on simple models of bars and spirals, selecting samples of 500 discrete tracers, to show that it is possible to measure pattern speeds with an average error of 17 per cent, and always better than 40 per cent, provided that asymmetry signals are sufficiently large, as described in Section 3. We then extracted a sample of some 250 OH/IR stars from the ATCA/VLA OH 1612-MHz survey and applied the method to these stars. This gave $\mathcal{K}/\mathcal{P} = 252 \pm 41\,\mathrm{km\,s^{-1}}$, from which we obtain $\Omega_p = 59 \pm 5\,\mathrm{km\,s^{-1}\,kpc^{-1}}$, with a possible systematic error of perhaps $10\,\mathrm{km\,s^{-1}\,kpc^{-1}}$, if $V_{\mathrm{LSR}} = 220\,\mathrm{km\,s^{-1}}$, $R_0 = 8$ kpc and $u_{\mathrm{LSR}} = 0$ (for other values of V_{LSR}, R_0 or u_{LSR}, Ω_p can be obtained from $\Omega_p R_0 - V_{\mathrm{LSR}} = 252 \pm 41 - 18u_{\mathrm{LSR}}$). The sample is quite small and the detection is only significant at about the 90 per cent level. Future, larger samples will improve this situation; we sketch how distance data combined with the projected position and line-of-sight velocity data used in our study will lead to a substantial improvement in our knowledge of the pattern speed(s) in the Milky Way Galaxy.

ACKNOWLEDGMENTS

This work was partly supported by grant # 20-56888.99 from the Swiss National Science Foundation. We thank the anonymous referee for comments which helped improve this paper.

REFERENCES

Amaral L. H., Lépine J. R. D., 1997, MNRAS, 286, 885
Backer D. C., Sramek R. A., 1999, ApJ, 524, 805
Beaulieu S. F., Freeman K. C., Kalnajs A. J., Saha P., Zhao H.-S., 2000, AJ, 120, 855
Bertin G., Lin C. C., 1996, Spiral Structure in Galaxies: A Density Wave Theory. The MIT Press, Cambridge
Bienaymé O., Bosma A., Athanassoula E., 1985, in Kahn F. D., ed., Cosmical Gas Dynamics. VNU Science Press, Utrecht, p. 205
Binney J., Gerhard O. E., Stark A. A., Bally J., Uchida K. I., 1991, MNRAS, 252, 210
Binney J., Gerhard O., Spergel D., 1997, MNRAS, 288, 365
Bissantz N., Gerhard O., 2002, MNRAS, 330, 591
Blitz L., Spergel D. N., 1991, ApJ, 370, 205
Buta R., 1995, ApJS, 96, 39
Canzian B., 1993, ApJ, 414, 487
Cohen R. J., Few R. W., 1976, MNRAS, 176, 495
Debattista V. P., Sellwood J. A., 1998, ApJ, 493, L5
Debattista V. P., Sellwood J. A., 2000, ApJ, 543, 704
Debattista V. P., Williams T. B., 2001, in Funes J. G., Corsini S. J., Corsini E. M., eds, ASP Conf Ser. Vol. 230, Galaxy Disks and Disks Galaxies. Astron. Soc. Pac., San Francisco, p. 553

Debattista V. P., Corsini E. M., Aguerri J. A. L., 2002, MNRAS, 332, 65
Deguchi S., Nakashima J.-I., Balasubramanyam R., 2001, PASJ, 53, 305
Dehnen W., 1999, ApJ, 524, L35
Dehnen W., Binney J. J., 1998, MNRAS, 298, 387
de Vaucouleurs G., 1964, in Kerr F. J., Rodgers A. W., eds, The Galaxy and The Magellanic Clouds. Aust. Acad. Sci., Sydney, p. 88
Drimmel R., Spergel D. N., 2001, ApJ, 556, 181
Dwek E. et al., 1995, ApJ, 445, 716
Elitzur M., Goldreich P., Scoville N., 1976, ApJ, 205, 384
Englmaier P., Gerhard O. E., 1999, MNRAS, 304, 512
Evans N. W., Read J. C. A., 1998, MNRAS, 300, 106
Fux R., 1999, A&A, 345, 787
Gerhard O., 2001, in Funes J. G., Corsini S. J., Corsini E. M., eds, ASP Conf Ser. Vol. 230, Galaxy Disks and Disks Galaxies. Astron. Soc. Pac., San Francisco, p. 21
Gerhard O. E., Vietri M., 1986, MNRAS, 223, 377
Gerssen J., Kuijken K., Merrifield M. R., 1999, MNRAS, 306, 926
Habing H. J., 1996, A&AR, 7, 97
Habing H. J., Tignon J., Tielens A., 1994, A&A, 286, 523
Hammersley P. L., Garzón F., Mahoney T. J., López-Corredoira M., Torres M. A. P., 2000, MNRAS, 317, L45
Honma M., Kawaguchi N., Sasao T., 2000, SPIE, 4015, 624
Kuijken K., Tremaine S., 1991, in Sundelius B., ed., Dynamics of Disc Galaxies. Göteborg, Sweden, p. 71
Kuijken K., Tremaine S., 1994, ApJ, 421, 178
Le Squeren A. M., Sivagnanam P., Dennefeld M., David P., 1992, A&A, 254, 133
Lindblad P. A. B., Kristen H., 1996, A&A, 313, 733
Lindblad P. A. B., Lindblad P. O., Athanassoula E., 1996, A&A, 313, 65
Liszt H. S., Burton W. B., 1980, ApJ, 236, 779
Merrifield M. R., Kuijken K., 1995, MNRAS, 274, 933
Mishurov Y. N., Zenina I. A., 1999, A&A, 341, 81
Morgan S., 1990, PASP, 102, 102
Mulder W. A., Liem B. T., 1986, A&A, 157, 148
Nakada Y., Onaka T., Yamamura I., Deguchi S., Hashimoto O., Izumiura H., Sekiguchi K., 1991, Nat, 353, 140
Nikolaev S., Weinberg M. D., 1997, ApJ, 487, 885
Paczynski B., Stanek K. Z., Udalski A., Szymanski M., Kaluzny J., Kubiak M., Mateo M., Krzeminski W., 1994, ApJ, 435, L113
Peters W. L., 1975, ApJ, 195, 617
Radhakrishnan V., Sarma V. N. G., 1980, MNRAS, 85, 249
Reid M. J., Readhead A. C. S., Vermeulen R. C., Treuhaft R. N., 1999, ApJ, 524, 816
Renzini A., 1981, in Iben I., Renzini A., eds, Astrophys. Space Sci. Library Vol. 88, Physical Processes in Red Giants. Reidel, Dordrecht, p. 431
Rix H.-W., Zaritsky D., 1995, ApJ, 447, 82
Sanders R. H., Huntley J. M., 1976, ApJ, 209, 53
Sellwood J. A., Sparke L. S., 1988, MNRAS, 231, 25
Sevenster M. N., 1996, in Buta R., Crocker D. A., Elmegreen B. G., eds, ASP Conf Ser. Vol. 91, Barred Galaxies, IAU Colloq. 157. Astron. Soc. Pac., San Francisco, p. 536
Sevenster M. N., 1999, MNRAS, 310, 629
Sevenster M. N., 2002, AJ, 123, 2788
Sevenster M. N., Kalnajs A., 2001, AJ, 122, 885
Sevenster M. N., Chapman J. M., Habing H. J., Killeen N. E. B., Lindqvist M., 1997a, A&AS, 122, 79
Sevenster M. N., Chapman J. M., Habing H. J., Killeen N. E. B., Lindqvist M., 1997b, A&AS, 124, 509
Sevenster M., Dejonghe H., Caelenberg K. Van, Habing H., 2000, A&A, 355, 537
Sevenster M. N., van Langevelde H., Chapman J. M., Habing H. J., Killeen N. E. B., 2001, A&A, 366, 481
Stanek K. Z., Udalski A., Szymanski M., Kaluzny J., Kubiak M., Mateo M., Krzeminski W., 1997, ApJ, 477, 163
Sygnet J. F., Tagger M., Athanassoula E., Pellat R., 1988, MNRAS, 232, 733
Tagger M., Sygnet J. F., Athanassoula E., Pellat R., 1987, ApJ, L43
Toomre A., 1981, in Fall S. M., Lynden-Bell D., eds, The Structure and Evolution of Normal Galaxies. Cambridge Univ. Press, Cambridge, p. 111
Tremaine S., Weinberg M. D., 1984, ApJ, 282, L5
Vallée J. P., 1995, ApJ, 454, 119
Weiland J. L. et al., 1994, ApJ, 425, 81
Weiner B. J., Sellwood J. A., 1999, ApJ, 524, 112
Weiner B. J., Sellwood J. A., Williams T. B., 2001, ApJ, 546, 931
Whitelock P. A., Catchpole R., 1992, in Blitz L., ed., The Centre, Bulge, and Disk of the Milky Way. Kluwer, Dordrecht, p. 103
Whitelock P. A., Feast M., 1993, in Weinberger R., Acker A., eds, Proc. IAU Symp. 155, Planetary Nebulae. Reidel, Dordrecht, p. 251
Zhao H.-S., Rich R. M., Spergel D. N., 1996, MNRAS, 282, 175

This paper has been typeset from a TEX/LATEX file prepared by the author.